

The role of size in the multiple scattering correction C for dual-spot aethalometer: a field and laboratory investigation

Laura Renzi¹, Claudia Di Biagio², Johannes Heuser³, Marco Zanatta^{1,2}, Mathieu Cazaunau³, Antonin Bergé², Edouard Pangui³, Jérôme Yon⁴, Tommaso Isolabella^{5,6}, Dario Massabò^{5,6}, Virginia Vernocchi⁶, Martina Mazzini¹, [Franziska Vogel](#)¹, Chenjie Yu², Paola Formenti², Benedicte Picquet-Varrault³, Jean-Francois Doussin³, Angela Marinoni¹

¹ Institute of Atmospheric Sciences and Climate, National Research Council of Italy, Bologna, Italy

² Université Paris Cité and Univ Paris Est Creteil, CNRS, LISA, F-75013 Paris, France

³ Univ Paris Est Creteil and Université Paris Cité, CNRS, LISA, F-94010 Créteil, France

⁴ INSA Rouen Normandie, Univ. Rouen Normandie, CNRS, Normandie Univ., CORIA UMR 6614, 76000, Rouen France

⁵ Department of Physics, University of Genoa, Via Dodecaneso 33, 16146 Genoa, Italy

⁶ INFN – Division of Genoa, Via Dodecaneso 33, 16146 Genova, Italy

Correspondence to: Laura Renzi (l.renzi@isac.cnr.it)

Abstract. The dual-spot aethalometer AE33 is a widely used instrument for measuring the aerosol absorption coefficient, but the accuracy of its measurements is heavily dependent on the multiple scattering correction factor (C), which compensates for multiple scattering effects in the filter matrix. ~~Despite its widespread use, the factors influencing variability of C remain poorly understood, particularly in relation to aerosol properties.~~ Despite its widespread use, several aspects influencing the variability of C, particularly those related to aerosol microphysical properties, are still not fully constrained.

In this work, we explore the variability of C for the AE33 in a wide range of conditions and aerosol properties by combining chamber experiments with freshly emitted laboratory-generated soot and ambient data from a mountaintop site in Italy (Monte Cimone, CMN). The C factor is derived by comparison with independent filter-based instruments such as the MAAP (Multi-Angle Absorption Photometer) and MWAA (Multi-Wavelength Absorption Analyzer) at CMN and the extinction-minus-scattering (EMS) approach in chamber experiments.

The mean C value at a wavelength of 637 nm derived at CMN is 2.35 with a standard deviation of 0.58, while the average values obtained in chamber experiments in different conditions range from 2.89 ± 0.03 to 3.9 ± 0.06 . The variability of C at CMN appears to be primarily influenced by the signal-to-noise ratio of the instruments, especially during the colder months when absorption coefficient values fall below 1 Mm^{-1} . In contrast, in the chamber experiments, the variability is mainly driven by particle properties. The C value at 637 nm, derived from measurements at CMN, increases with increasing single scattering albedo (SSA), particularly for SSA values above 0.94, while showing no statistically significant spectral variability. ~~Both ambient and chamber experiments highlight the dependence of the C factor on particle size, with C increasing as particle diameter decreases below 120 nm. This size dependence is relatively small (within 15%) under ambient conditions dominated by mostly scattering aerosols, but it leads to changes greater than 60% for highly absorbing soot particles.~~ Both ambient and chamber experiments highlight the dependence of the C factor on particle size, with C increasing as particle diameter decreases below 200 nm. This size dependence is relatively small (within 25%) under ambient conditions dominated by mostly scattering aerosols, but it leads to changes greater than 60%

43 [for highly absorbing soot particles. These results are relevant for improving the accuracy and comparability of aerosol](#)
44 [absorption measurements performed by aethalometers, particularly within monitoring networks. The observed](#)
45 [dependence of C on particle size suggests that differences between urban and remote sites, or between periods dominated](#)
46 [by nucleation versus coarse-mode particles \(e.g., dust\), may contribute to the variability reported across locations.](#)
47 [Understanding these dependencies is essential for refining correction approaches and reducing inter-site discrepancies in](#)
48 [network datasets.](#)

49 **1 Introduction**

50 Absorbing aerosols have a unique and important role in the Earth's climate system (Bond et al., 2013; Liu et al., 2020a).
51 By absorbing solar and terrestrial infrared radiation, aerosols exert an influence on low tropospheric temperature, liquid
52 and ice cloud distribution and properties, atmospheric dynamics, as well as surface reflectivity, in particular over snow
53 and ice surfaces (Ramanathan and Carmichael, 2008; Liu et al., 2020a; Li et al., 2022; Kok et al., 2023). This impact is
54 especially significant for strongly absorbing species such as black carbon (BC), brown carbon (BrC), and mineral dust.
55 These components account for the majority of aerosol light absorption and contribute substantially to the direct radiative
56 effect at both regional and global scales (e.g. Chung et al., 2012; Kok et al., 2023; Sand et al., 2021; Zhu et al., 2021).

57 The strength of this radiative effect is typically characterized by the aerosol absorption coefficient, expressed in inverse
58 mega meters (b_{abs} , Mm^{-1}) that represents the amount of light absorbed by aerosol per unit volume. The b_{abs} is commonly
59 measured using filter-based techniques, differential extinction-minus-scattering (EMS) methods, or photoacoustic
60 instruments. Despite its importance, aerosol absorption remains poorly constrained. This is primarily due to the lack of
61 standardized measurement approaches and the presence of instrument-specific biases (Petzold et al., 2013), which
62 introduce substantial uncertainties in b_{abs} data. In consequence, a major difficulty lies in capturing the magnitude and
63 spatio-temporal variability of the spectral mass absorption cross section (MAC, m^2g^{-1}), i.e. the absorption coefficient per
64 unit of absorbing specie mass concentration ($\mu\text{g m}^{-3}$), or the single scattering albedo (SSA), representing the fraction of
65 scattered radiation with respect to extinction. The MAC and SSA depend on a wide variety of variables such as the
66 composition (via the complex refractive index, CRI), size, morphology and mixing state of the particles (Liu et al., 2020b;
67 Moteki, 2023). Understanding these dependencies is required for a better representation of absorbing aerosols in climate
68 models and remote sensing algorithms (e.g., Samset et al., 2018). In this regard, improving the accuracy of in situ
69 measurements of the spectral aerosol absorption coefficient b_{abs} is fundamental for contributing to robust CRI, MAC and
70 SSA evaluation.

71 The Aethalometer (Hansen et al., 1984; Drinovec et al., 2015) is the most used instrument for routine measurements of
72 the aerosol absorption coefficient in the GAW (Global Atmospheric Watch) and ACTRIS-RI (Aerosol, Clouds, and Trace
73 gases Research Infrastructure; <https://www.actris.eu/>) observational networks (e.g., Laj et al., 2020; Savadkoobi et al.,
74 2023; Rovira et al., 2025), with a long-record of applications in ground-based and airborne intensive field campaigns (e.g.
75 Fialho et al., 2005; Sandradewi et al., 2008; Formenti et al., 2011; Di Biagio et al., 2016; Favez et al., 2021; Ohata et al.,
76 2021) and laboratory experiments (e.g. Weingartner et al., 2003; Baldo et al., 2023; Di Biagio et al., 2019; Kalbermatter
77 et al., 2022).

78 The aethalometer is a filter-based photometer. It measures the light attenuation (ATN) through a filter on which the
79 aerosol is continuously collected at a constant flow rate. The volume absorption coefficient is estimated via the Beer-
80 Bouguer-Lambert law based on the ATN rate of change over the time interval Δt (typically 1–2 minutes). This rate is

81 proportional to the absorbing aerosol concentration and it is also used to calculate an optically-equivalent BC mass
82 concentration (eBC, $\mu\text{g m}^{-3}$) using prescribed instrumental MAC spectral values (Petzold et al., 2013). The aethalometer
83 measurement technique has the advantage of being sensitive to low aerosol signals even for relatively low integration
84 times (e.g., Hansen et al., 1984) and so to be adapted to measurements in environments with variable aerosol loadings.
85 The aethalometer is also easily deployable and provides b_{abs} at seven wavelengths covering the broad range from 370 to
86 950 nm.

87 Despite its operational advantages, the aethalometer measurement is affected by environmental and aerosol-related
88 artefacts that can seriously bias the retrieved absorption coefficient (Arnott et al., 2005; Schmid et al., 2006; Virkkula et
89 al., 2015; Weingartner et al., 2003, hereafter referred as W2003; Collaud Coen et al., 2010, hereafter referred as C2010).
90 These are linked to three causes: 1. the accumulation of particles on the filter that reduces the linearity in the detected
91 attenuation signal, therefore causing an underestimate of the absorption coefficient for increasing aerosol deposition (the
92 loading effect); 2. the scattering from particles deposited on the filter that contributes to detected attenuation and that
93 causes an overestimation of the absorption (the scattering effect); 3. the multiple scattering by the filter fibers causing an
94 increased optical path and absorption overestimation (the multiple scattering effect).

95 Aethalometer models commercialized by Magee Scientific have evolved over time to address the known measurement
96 artefacts. Earlier models, such as the AE31, did not include any automatic correction for these effects. Instead, post-
97 processing algorithms and empirical correction factors—extensively studied and developed in the literature—were
98 required to compensate for biases such as loading, scattering, and multiple scattering (Weingartner et al., 2003; Arnott et
99 al., 2006; Bond and Bergstrom, 2006; Collaud Coen et al., 2010; Segura et al., 2014; Backman et al., 2017; Di Biagio et
100 al., 2017; Saturno et al., 2017).

101 The more recent AE33 model, includes a dual-spot system that automatically compensates for the loading effect in real
102 time (Drinovec et al., 2015). However, even in newer models, the correction for scattering and multiple scattering still
103 relies on the application of a scaling factor, typically referred to as C or C_{ref} . As of today, estimations of the C from various
104 field and laboratory studies have been performed, investigating aerosols of different types and properties and varying
105 ambient conditions (Corbin et al., 2018; Kim et al., 2019; Laing et al., 2020; Valentini et al., 2020; Moschos et al., 2021;
106 Yus-Díez et al., 2021; Bernardoni et al., 2021; Kalbermatter et al., 2022). These studies have reported a wide range of C
107 values, from about 2.26 to 8.26, which translates into significant uncertainty, as b_{abs} is inversely proportional to this factor.
108 This variability remains one of the major challenges in standardizing and comparing absorption measurements across
109 different studies and networks.

110 As of today, there is still no consensus on the appropriate value of C or its dependence on specific aerosol properties or
111 experimental conditions. The influence of parameters such as particle size, chemical composition, and spectral wavelength
112 on C remains debated. Particle size can lead to bias in the measurement of the absorption coefficient carried out with
113 filter-based instruments (Lack et al., 2009; Nakayama et al., 2010). This dependence is related to the different depth of
114 penetration of particles of different sizes into the filter, as well as to the characteristics of the filter (Hinds, 1999; Huang
115 et al., 2013; Berry et al., 2023). For the aethalometer, particle size has been suggested as a factor that could contribute to
116 the variability of C values across different locations and seasons (Bernardoni et al., 2021, Luoma et al., 2021), although
117 direct observational evidence for this dependence in the aethalometer AE33 remains limited (Drinovec et al., 2022;
118 [Romshoo et al., 2022](#); Yus-Díez et al., 2025). Regarding the composition, previous studies have demonstrated that the
119 optical properties of sampled particles can directly influence aethalometer measurements by altering the amount of
120 scattered light, which the instrument may incorrectly interpret as absorption. An increase in the SSA has been linked in

121 these studies to a corresponding rise in the C values (Schmid et al., 2006; Backman et al., 2017; Yus-Díez et al., 2021).
122 Moreover, very few studies have focused on C estimations for aerosol populations with high fractions of black and brown
123 carbon (BC and BrC), such as those found near combustion sources or in laboratory studies on combustion aerosols.

124 This uncertainty has practical implications, particularly for international observation networks like ACTRIS RI, which
125 currently recommend the use of a single, wavelength-independent C value. The objective of this study is to improve the
126 characterization of the C parameter for the AE33 aethalometer model, currently the most widely used. ~~Specifically, we
127 investigate its potential dependence on aerosol properties such as particle size, single scattering albedo (SSA), and
128 measurement wavelength. To capture a wide range of conditions, the analysis includes both field data from a mountain
129 observatory with highly variable aerosol loads and properties, and chamber experiments involving combustion-generated
130 soot with varying BC and BrC content under atmospherically relevant conditions.~~

131 Specifically, we examine its dependence on particle size, while also considering the effects of other properties such as
132 SSA and wavelength to support and complement existing evidence from the literature. The chamber experiments were
133 designed to explore a broader particle size range than in previous studies (Drinovec et al., 2022), taking advantage of
134 controlled conditions to better isolate the role of size and evaluate its relative importance compared to other aerosol
135 properties. These experiments were conducted using freshly generated soot and non-filter-based reference techniques,
136 ensuring independence from filter-related artifacts. Ambient observations, although subject to more variable and less
137 controlled conditions, were used to assess whether the dependence on particle size can also be observed under real
138 atmospheric conditions. This contributes additional context to previous work, where ambient investigations remain
139 limited (e.g., Yus-Díez et al., 2025).

140 Given the widespread use of aethalometers in long-term observational networks, constraining the variability of the C
141 factor is crucial for ensuring the quality and comparability of absorption data across sites. Differences in aerosol size
142 distributions and mixing states—such as between freshly emitted soot in urban areas and aged or coarse particles at remote
143 stations—can introduce systematic biases if a single, constant C is applied. A more robust understanding of these
144 dependencies is therefore required to guide the harmonization of network measurements and to support the development
145 of improved parameterizations for data correction.

146 **2 Methods**

147 The C dependencies were investigated through the synergic use of both chamber experiments and observational long term
148 data series. While ambient measurements are valuable for investigating the spatial and temporal variability of C in the
149 real atmosphere, chamber experiments provide a more controlled setting, where variability of multiple variables can be
150 minimized, enabling a clearer understanding of how the C-factor depends on specific particle properties.

151 This section provides description of the experimental setup for field and chamber experiments and description of C factor
152 calculations. A summary of the instruments considered in this study, including deployment details and availability, and
153 measurement uncertainties is provided in [Table 1](#) and [Table 2](#). All volumetric quantities used in the analysis
154 were converted to standard temperature and pressure conditions (STP), assuming 1013.25 mbar and 273.15 K.

155 **2.1 Experimental set-up**

156 **2.1.1 Field measurements at Mt Cimone**

157 Field measurements were carried out at the mountain site of Monte Cimone (CMN, Italy, 44°11'N-10°42'E, 2165 m
158 a.s.l.), located in northern Italy near the Po Valley. The CMN observatory is situated on the summit of the highest
159 mountain in the northern Apennines, and its orographic features allow air masses to arrive from all directions, making it
160 representative of a relatively pristine atmosphere. However, particularly during summer and midday hours, it may be
161 subject to the uplift of pollutants due to planetary boundary layer (PBL) rise and valley breezes (Marinoni et al., 2008;
162 Cristofanelli et al., 2009; Andrews et al., 2011; Cristofanelli et al., 2018). The site is also subject to Saharan dust intrusions
163 (Vogel et al., 2025) and the long-range transport of wildfire emissions throughout the year (Cristofanelli et al., 2009,
164 2024). These diverse conditions affect aerosol properties, including particle size (e.g., following dust transport or new
165 particle formation events; Vogel et al. 2025) as well as their optical and chemical characteristics, influenced by sources
166 such as the Po Valley, wildfires, and dust.

167 The CMN station is part of the World Meteorological Organization's (WMO) Global Atmosphere Watch (GAW) program
168 and high-quality routine measurements of major aerosol properties are conducted in accordance with the ACTRIS-RI
169 guidelines. This study presents measurements collected between July 2020 and November 2022. Aerosols were sampled
170 through a TSP (Total Suspended Particles) inlet, specifically designed for high mountain stations.

171 The spectral absorption coefficient was measured using a dual-spot AE33 aethalometer (RH < 40% ensured by a Nafion®
172 dryer), and complemented by reference absorption techniques: the Multi-Angle Absorption Photometer (MAAP, online,
173 637 nm, Thermo Sci.; Petzold and Schönlinner, 2004) and the Multi-Wavelength Absorption Analyzer (MWAA, offline,
174 5 wavelengths, 375-405-532-635-870 nm, Massabò et al., 2015). The scattering coefficient was measured with an
175 integrating nephelometer (TSI Inc., model 3563, Anderson et al., 1996; Massoli et al., 2009).

176 **2.1.2 Simulation experiments in the CESAM chamber**

177 Chamber experiments were performed in controlled conditions in the 4.2 m³ stainless-steel multi-instrumented CESAM
178 chamber (French acronym for Experimental Multiphase Atmospheric Simulation Chamber, <https://cesam.cnrs.fr/>; Wang
179 et al., 2011), which has been extensively used in recent years to simulate the formation and aging of different types of
180 aerosols and investigate their physico-chemical and spectral optical properties (Denjean et al., 2015; Di Biagio et al.,
181 2017, 2019; De Haan et al., 2020; Baldo et al., 2023).

182 The experiments were performed during three campaigns occurred in May 2021, October 2021 and December 2022 and
183 involved primary combustion BC- and BrC-containing soot aerosols. Full detailed description of the setup and data
184 analysis for those experiments is provided in Heuser et al. (2025⁴).

185 Soot aerosols with varying BC and BrC content were generated by a computer-controlled miniCAST burner (model
186 6204C, Jing Ltd., Switzerland). The miniCAST is a co-flow diffusion flame generator. It produces soot aerosols (hereafter
187 identified as cast soot, CS) by burning a mixture of propane (C₃H₈), N₂ and oxidation air. Varying the proportions of these
188 gases allows to vary the size, composition and morphology of the generated CS particles (e.g. Moore et al., 2014; Bescond
189 et al., 2016). In this study five different miniCAST operation points were investigated, corresponding to four fuel-lean
190 burning conditions (CS1-CS4) and one fuel-rich condition (CS5) (Table S1). The CS aerosol particles were injected in
191 CESAM via a charcoal denuder to remove volatile organic compounds possibly present in the miniCAST exhaust. After

192 injection in the chamber, the CS was left in suspension to age under different controlled conditions. In this work we only
 193 consider experiments in which CS is aged under dry conditions for aging times between 2 and 6 hours.

194 Between experiments, the chamber was mechanically evacuated and pumped to $3 \cdot 10^{-4}$ mbar for at least a few hours and
 195 usually over a full nighttime period. In addition to overnight evacuation, the chamber was manually cleaned at the
 196 beginning of each campaign. Background concentrations of aerosols in the chamber were usually less than $0.05 \mu\text{g m}^{-3}$
 197 (that is nearly 10^4 times less than the injected CS mass concentration in the chamber reaching up to 60 to $95 \mu\text{g m}^{-3}$). The
 198 different experimental conditions for chamber experiments are summarized in Table S1 and S2. For the majority of
 199 experiments several repetitions are performed to test the reproducibility of results.

200 The spectral absorption coefficient was measured in CESAM by means of a dual spot aethalometer AE33, complemented
 201 by the extinction–minus–scattering (EMS) approach (Onasch et al., 2015; Modini et al., 2021) as reference absorption
 202 technique. The extinction coefficient was measured by means of a CAPS PMex instrument (Aerodyne, Massoli et al.,
 203 2010) and the scattering coefficient by an integrating nephelometer (TSI Inc., model 3563, Anderson et al., 1996; Massoli
 204 et al., 2009).

205 2.2 Quantification of C factor for the dual spot aethalometer

206 The aethalometer measures the attenuation coefficient $b_{\text{atn}}(\lambda)$ which is proportional to the light attenuation (ATN) rate of
 207 change over time. The multiple scattering correction factor C is defined as:

$$208 \quad C(\lambda) = \frac{b_{\text{atn},\text{LC}}(\lambda)}{b_{\text{abs},\text{ref}}(\lambda)} \quad (1)$$

209 where $b_{\text{atn},\text{LC}}$ is the attenuation coefficient measured by the aethalometer and corrected for the loading effect based on the
 210 AE33 automatic internal algorithm, described in the next section, and $b_{\text{abs},\text{ref}}$ is the reference absorption coefficient.

211 2.2.1 Dual-spot aethalometer loading correction

212 The model AE33 automatically corrects for the loading effect, through an internal algorithm, by measuring the change in
 213 light attenuation in two filter spots, crossed by different air flows, therefore with different aerosol loads. The ATN
 214 measurements from the two spots are combined through a set of equations detailed in Drinovec et al. (2015) to provide
 215 as output the $e\text{BC}_{\text{AE33}}$ based on the following formulation:

$$216 \quad e\text{BC}_{\text{AE33}}(\lambda) = \frac{S \cdot \left(\frac{\Delta\text{ATN}_1(\lambda)}{100} \right)}{F_1(1 - \zeta) \cdot \text{MAC}_{\text{AE33}}(\lambda) \cdot C_{\text{instr}} \cdot (1 - k(\lambda) \cdot \text{ATN}_1(\lambda)) \cdot \Delta t} \quad (2)$$

217 where S is the spot surface area (m^2), ΔATN_1 is the variation of attenuation through the filter spot1 (that is the one with
 218 the highest flow rate) in the time interval Δt , F_1 is the flow rate through spot1 ($\text{m}^3 \text{min}^{-1}$), ζ is the flow leakage (taking into
 219 account lateral flow in the filter matrix), $\text{MAC}_{\text{AE33}}(\lambda)$ is the instrumental mass absorption cross section (18.47, 14.54,
 220 13.14, 11.58, 10.35, 7.77, 7.19 $\text{m}^2 \text{g}^{-1}$ at 370, 470, 520, 590, 660, 880, 950 nm, respectively), and $k(\lambda)$ is a corrective
 221 parameter derived by the instrument algorithm to automatically account for the loading effect. As indicated in Eq. (2) the
 222 algorithm also accounts for an instrumental multi scattering correction $C_{\text{instr,AE33}}$ (wavelength-independent) for
 223 harmonization among aethalometers using different tape materials (quartz, TFE-coated glass; Drinovec et al., 2015). The
 224 $C_{\text{instr,AE33}}$ value depends on the filter material and is 1.39 for the for the M8060 filter tape used in this study. Starting from
 225 Eq. (2) the spectral loading–corrected attenuation coefficient $b_{\text{atn},\text{LC}}(\lambda)$ is derived from $e\text{BC}_{\text{AE33}}$ data by multiplying for the
 226 default instrumental $C_{\text{instr,AE33}}$ and the $\text{MAC}_{\text{AE33}}(\lambda)$ as:

$$b_{atn,LC,AE33}(\lambda) = eBC_{AE33}(\lambda) \cdot MAC_{AE33}(\lambda) \cdot C_{instr,AE33} \quad (3)$$

As previously noted by Cuesta-Mosquera et al. (2021), the automatic AE33 loading correction method has limitations, particularly around filter changes, potentially introducing biases. These limitations are particularly critical when absorbing aerosol concentration is high, filter changes frequent (tens of minutes-few hours), and experiment durations relatively short. At CMN, where the concentration of absorbing species is typically low ($0.2 \mu\text{g m}^{-3}$), the filter changes occur after several hours or days. Conversely, for chamber experiments, the higher soot concentration leads to frequent filter changes (tens of minutes-few hours). In the present analysis, both for field measurements and chamber experiments, the internal correction automatically applied by the instrument was utilized. For field measurements, the $b_{atn,LC}(\lambda)$ values obtained at 1-minute resolution from the $eBC(\lambda)$ values provided by the instrument were averaged over one hour. Conversely chamber data, for which experiment duration is limited, were analysed at 1-min resolution. A detailed discussion on the effect of high soot concentrations on the loading correction for the AE33 $b_{atn,LC}(\lambda)$ calculation and C evaluation for chamber experiments is provided in the Supplementary Information (Text S1 and S2).

2.2.2 Reference absorption coefficient at CMN: filter-based MAAP and MWAA

The MAAP and the MWAA are the filter-based reference instruments used at CMN. The MAAP is based on the simultaneous measure of both the reflected and the transmitted light of aerosols embedded in a filter. An algorithm based on the Mie theory and the two stream approximation is then used to convert these signals in values of SSA_{PF} and optical thickness ($\tau_{PF} = \ln(T_{PF})$) of the particle-filter (PF) system. These parameters allow to retrieve the aerosol absorption coefficient using the equation:

$$b_{abs,ref} = \frac{S}{V} ABS = -\frac{S}{V} (1 - SSA_{PF}) \ln(T_{PF}) \quad (4)$$

where S is the spot surface area (m^2) of collection and V the sampled volume of air (m^3). The basic principle of the MWAA technique is based on the MAAP concept. However, while the MAAP is a field-deployable instrument working at a single wavelength (637 nm), the MWAA is a laboratory-based setup that extends the principle of the MAAP to 5 wavelengths and analyze filter aerosol samples. Because of their different nature, the MAAP is a high resolution instrument (with observations typically every minute) while the MWAA integrates observations across an aerosol sampling period that can be variable depending on the concentrations (minutes to hours).

The MAAP is routinely measuring at the CMN site collecting data of $b_{abs,ref}$ at 637 nm at 1-min time resolution. Data measured in the period from July 2020 to November 2022 are considered in this study. The MWAA technique was instead used to measure the $b_{abs,ref}$ at 5 different wavelengths on 43 samples collected every 24 hours by the MAAP at CMN in the period September-October 2022.

The absorption coefficient measured by the MAAP at 637 nm ($b_{abs,ref}$) was averaged over the same 1-h intervals as the AE33 data and used to derive the C factor at 637 nm according to Eq. (1). For consistency in wavelength, before calculating the C factor, the AE33 attenuation coefficient ($b_{atn,LC}$) measured at 660 nm was interpolated to 637 nm using the Absorption Ångström Exponent (AAE) obtained from the power-law fit of $b_{atn,LC}(\lambda)$ versus wavelength.

261 The spectral dependence of C was analysed using MWAA measurements. In this case, the reference absorption
262 coefficients $b_{\text{abs,ref}}(\lambda)$ were interpolated to the AE33 wavelengths. C values were then calculated at the seven AE33
263 wavelengths by averaging the AE33 $b_{\text{attn,LC}}(\lambda)$ data over the 24 h corresponding to each MWAA filter sample.

264
265 ~~The $b_{\text{abs,ref}}$ at 637 nm measured by the MAAP were averaged over the same 1-h step of the AE33 and used to estimate the~~
266 ~~C at 637 nm based on Eq. (1). The AE33 $b_{\text{attn,LC}}$ data at 637 nm were interpolated at 637 nm using the absorption Ångström~~
267 ~~exponent (AAE) calculated as the power-law fit of $b_{\text{attn,LC}}(\lambda)$ vs the wavelength ($b_{\text{attn,LC}} \sim \lambda^{-AAE}$).~~
268 ~~The $b_{\text{abs,ref}}(\lambda)$ measured by the MWAA was used to study the spectral dependence of C. Values of C were calculated at~~
269 ~~the 7 λ of the aethalometer, averaging $b_{\text{attn,LC}}(\lambda)$ over the same 24 hours of MWAA samples and interpolating the $b_{\text{abs,ref}}(\lambda)$~~
270 ~~at the AE33 wavelengths ($b_{\text{abs,ref}} \sim \lambda^{-AAE}$).~~

271 **2.2.3 Reference absorption coefficient at CESAM: extinction-minus-scattering approach**

272 The EMS approach is considered as reference absorption technique for chamber experiments. This method involves the
273 simultaneous measurements of both the extinction (b_{ext}) and scattering coefficient (b_{sca}) and the absorption coefficient is
274 obtained as the difference of the two. When applied in the field to predominantly scattering samples, this technique is
275 affected by high level of uncertainty as discussed in Modini et al. (2021). However, it can be successfully used as a good
276 standard in laboratory experiments with high absorption signals. Validation of the methodology is provided in Heuser et
277 al. (20254). In this study the extinction coefficient at 630 nm was measured by means of a CAPS PMex instrument
278 (Aerodyne, Massoli et al., 2010). Extinction coefficient measured from the CAPS PMex does not require further
279 adjustments. The scattering coefficient at 450, 550, and 700 nm was measured by an integrating nephelometer (TSI Inc.,
280 model 3563, Anderson et al., 1996). The nephelometer b_{sca} needs to be corrected for truncation, in order to compensate
281 for the limited field of view of the instrument. The truncation correction was calculated using the Massoli et al. (2009)
282 approach adapted to highly absorbing aerosols as those probed in chamber experiments, as discussed in Heuser et al.
283 (20254). Assumptions on the real refractive index are required in the Massoli et al. (2009) calculation. For the different
284 experiments considered in this study the real index was set at $n=1.9$, based on the proposed CRI for fresh BC by Bond
285 and Bergstrom (2006). A sensitivity test was performed to investigate the potential error caused by this assumption.
286 Changes in the corrected scattering signal for a range of likely real parts was found to be 4%.

287 The truncation-corrected b_{sca} values were interpolated at 630 nm based on the Scattering Ångström Exponent (SAE)
288 calculated as the power-law fit of b_{sca} vs the wavelength ($b_{\text{sca}} \sim \lambda^{-SAE}$). The b_{abs} at 630 nm was calculated at 1-min resolution
289 as the difference of the CAPS-PMex b_{ext} and the nephelometer b_{sca} . The C values at 630 nm were derived at 1-minute
290 resolution and then averaged over each aethalometer filter spot.

291 **2.3 Ancillary measurements**

292 **2.3.1 Single scattering albedo (SSA)**

293 The aerosol SSA was calculated at 637 nm and 1-hour resolution at CMN and at 630 nm at 1-minute resolution for
294 chamber experiments, as:

$$295 \quad \text{SSA} = \frac{b_{\text{sca}}}{b_{\text{ext}}} \quad (5)$$

296 The b_{sca} was measured at 450 nm, 550 nm, and 700 nm by the TSI nephelometer both in field and in the chamber. At
297 CMN the nephelometer data were corrected for truncation effects following the method of Anderson and Ogren (1998)

298 and extrapolated at 637 nm as ($b_{sca} \sim \lambda^{-SAE}$). Only measurements taken at relative humidity levels below 40% were
 299 considered. The b_{ext} in Eq. (5) was calculated as ($b_{sca} + b_{abs,ref}$) at CMN, while retrieved from CAPS PMex data in the
 300 chamber.

301 2.3.2 Particle size distribution

302 The particle number size distribution ($dN/d\log D_m$; D_m , mobility diameter), in the range of diameters from 10 to 800 nm,
 303 was measured at CMN by using a scanning particle mobility sizer (SMPS-TROPOS), operating at 5-minutes resolution
 304 and at 5/1 l min⁻¹ sheath/aerosol flow rates. In chamber experiments the particle number size distribution, was instead
 305 measured in the range of diameters from 19.5 to 881.7 nm, by using a scanning particle mobility sizer (TSI SMPS)
 306 consisting in an ⁸⁵Kr neutralizer, a Differential Mobility Analyzer (DMA, model 3080, TSI Inc.), and a Condensation
 307 Particle Counter (CPC, model 3772, TSI Inc.), operated at 2.0/0.2 l min⁻¹ sheath/aerosol flow rates, and at a time resolution
 308 of 3 minutes. Measurements were corrected for diffusion losses and multiple charge effects with the instrument software.

309 ~~The size distribution measured by the SMPS was used to derive the geometric mean diameter ($D_{m,geo}$) through the~~
 310 ~~following equation:~~

$$311 \ln(D_{m,geo}) = \frac{\sum_{i=m}^n \Delta N_i \cdot \ln(d_i)}{N} \quad (6)$$

312 ~~where d_i is the midpoint diameter for size channel i , N is the total concentration, ΔN_i is the particle concentration within~~
 313 ~~channel i , m is the first channel, and n is the last channel. The equation was applied to hourly averaged size distributions~~
 314 ~~at CMN and to both 3 minutes size distributions and size distribution averaged on each filter spot of the aethalometer in~~
 315 ~~chamber experiments. The uncertainty associated to the geometric mean diameter was the geometric standard deviation.~~
 316 ~~To notice that in the field the size distribution is multi-modal and include both absorbing and non-absorbing particles, in~~
 317 ~~chamber experiments they were mono-modal and including only absorbing aerosols.~~

319 The size distribution measured by the SMPS was used to derive the volume mean mobility diameter ($D_{m,vol}$). This
 320 parameter was derived from hourly averaged size distributions at CMN and to both 3-minutes size distributions and size
 321 distribution averaged on each filter spot of the aethalometer in chamber experiments.

322 To notice that in the field the size distribution is multi-modal and include both absorbing and non-absorbing particles, in
 323 chamber experiments they were mono-modal and including only absorbing aerosols.

324 **Table 1:** Datasets and optical instruments deployed for field observations at Cimone (CMN) and CESAM chamber experiments.

Site	Period	Optical instrumentation
CMN	July 2020 - November 2022	AE33, MAAP, nephelometer
	September - October 2022	AE33, MAAP, MWAA, nephelometer
	May 2021	
CESAM	October 2021	AE33, CAPS Pmex, nephelometer
	December 2022	

326

327

Table 2: Technical details of the instruments used in the present analysis.

Instrument	Wavelengths (nm)	Percent uncertainty	Reference	Flow rate (l min ⁻¹)		Temporal resolution		Size range (nm)	
				CMN	CESAM	CMN	CESAM	CMN	CESAM
Aethalometer (model AE33, Magee Sci.)	370, 470, 520,	± 24 %	Drinovec et al. (2015)	5	2	1 min	1 min	-	-
	590, 660, 880, 950		Mosquera et al. (2021)						
Multi-Angle Absorption Photometer MAAP (model 5012, Thermo Sci.)	637	±12%	Petzold and Schönlinner (2004) Petzold et al. (2005)	17	-	1 min	-	-	-
Multi-Wavelength Absorption Analyzer (MWAA, custom-made)	375, 405, 532, 635, 850	± 3-20 %	(Massabo et al., 2013)	-	-	24 hours	-	-	-
Nephelometer (model 3563, TSI Inc.)	450, 550, 700	± 8 %	Anderson (1996) Anderson and Ogreen (1998) Massoli et al. (2009)	35	2	1 min	1 sec	-	-
Cavity Attenuated Phase Shift Extinction (CAPS PMex, Aerodyne)	450, 630	± 6%	Massoli et al. (2010)	0.85	-	-	1 sec	-	-
SMPS	-	<u>±10%</u>	(Wiedensohler et al., 2012)	5	2	5 min	3 min	10-800	19.5-881.7

331 3 Results

332 3.1 Investigating C dependence on particle properties with chamber experiments

333 The experiments in the CESAM simulation chamber, presented in this study, were designed to investigate the specific
334 dependence of the C-factor on the chemical and physical properties of highly absorbing BC-containing soot particles. The
335 five different cast soot (CS) studied in the present work correspond to four fuel-lean burning conditions (CS1–CS4) and
336 one fuel-rich condition (CS5) leading to particles with a decreasing EC/TC ratio (0.79 ± 0.11 for CS1 to 0.00 ± 0.22 for
337 CS5) and decreasing number median diameter (from an average of 145 ± 12 nm for CS1 to 79 ± 2 nm for CS5, expressed
338 as mobility diameter (Heuser et al., 20254)).

339 3.1.1 Average chamber C value and the role of loading correction

340 The average values of C and their corresponding uncertainties for each experimental condition in the chamber are
341 summarized in Table 3. These values range from 2.89 ± 0.03 to 3.9 ± 0.06 , with the highest values corresponding to CS5,
342 which is characterized by a higher organic content and smaller particle sizes. The lowest values correspond to CS1, which
343 has a higher content of elemental carbon and larger particle sizes. The C values obtained for soot in the chamber
344 experiments are similar, considering the uncertainties, to the values reported in other studies from the urban site of Milan
345 (Bernardoni et al., 2021; Ferrero et al., 2021) and laboratory experiments using soot generated with a miniCAST burner
346 (Kalbermatter et al., 2022).

347 Due to the high concentration of absorbing soot, the possible dependence of the retrieved C on the loading correction
348 scheme was also evaluated. Indeed, in case of high absorbing aerosols concentration and frequent filter changes, the
349 internal AE33 correction can provide uncertain results. The time variability of the $b_{\text{atm,LC}}$ may in some cases not to follow
350 the same decreasing trend over time as the reference measurement. However, it showed a steeper decline before and after
351 the filter change, with a more rapid decrease in these points, making the trend appear more abrupt and also discontinuous
352 around the filter transition. ~~In these cases, the AE33 data can be re-corrected for loading effect. With this aim, the AE33~~
353 ~~can be treated like a single spot aethalometer and the loading correction schemes from W2003 or C2010 be applied. In~~
354 ~~these cases, the AE33 data can be re-corrected for loading effect. With this aim, the AE33 can be treated like a single-~~
355 ~~spot aethalometer and the loading correction schemes from W2003 and C2010, or the Dual Spot aethalometer method~~
356 ~~itself with a constant compensation parameter, be applied.~~ In the present analysis we tested the impact of different loading
357 correction schemes on C retrieval and found that the method applied to correct loading can introduce differences of
358 maximum 30% in the average values. Despite not impacting the conclusion of the present study, the role of loading effect
359 and correction scheme on retrieved C and b_{abs} should be taken into consideration. A detailed discussion of this specific
360 analysis is provided in Supplementary Information.

362 **Table 3:** Average C values for each soot type (CS1–CS5) and associated particles properties. In particular, the average geometric mean
363 diameter ($D_{\text{m,geo}}$), absorption coefficient b_{abs} and single scattering albedo (SSA). These values were derived averaging the results
364 obtained for all aethalometer filter spots corresponding to the same CS type. Values obtained in this study are shown together with the
365 ratio between elemental and total carbon mass concentration (EC/TC) and the Absorption Ångstrom Exponent (AAE) derived in Heuser
366 et al. (2024). Average C values for each soot type (CS1–CS5) and associated particles properties. In particular, the average volume
367 mean diameter ($D_{\text{m,vol}}$), absorption coefficient b_{abs} and single scattering albedo (SSA). These values were derived averaging the results
368 obtained for all aethalometer filter spots corresponding to the same CS type. Values obtained in this study are shown together with the
369 ratio between elemental and total carbon mass concentration (EC/TC) and the Absorption Ångstrom Exponent (AAE) derived in Heuser
370 et al. (20254).

C (630 nm)	$D_{\text{m,vol}}$ [nm] (this study)	b_{abs} [Mm^{-1}] (this study)	SSA (630 nm)	AAE	EC/TC
---------------	---	---	-----------------	-----	-------

	(this study)			(this study)	(Heuser et al., 2025 ⁴)	(Heuser et al., 2025 ⁴)
CS1	2.89 ± 0.03	<u>351.5 ± 15.9</u>	450 ± 30	0.08 ± 0.01	1.27 ± -0.13	0.79 ± 0.11
CS2	3.00 ± 0.03	<u>291.0 ± 18.2</u>	179 ± 11	0.09 ± 0.01	1.36 ± -0.21	0.73 ± 0.08
CS3	2.96 ± 0.03	<u>339.9 ± 18.8</u>	400 ± 30	0.09 ± 0.01	1.59 ± -0.22	0.67 ± 0.09
CS4	2.99 ± 0.03	<u>273.2 ± 18.3</u>	59 ± 4	0.08 ± 0.01	1.88 ± -0.31	0.53 ± 0.13
CS5	3.90 ± 0.06	<u>181.2 ± 16.5</u>	63 ± 6	0.29 ± 0.03	3.79 ± -0.33	0.00 ± 0.22

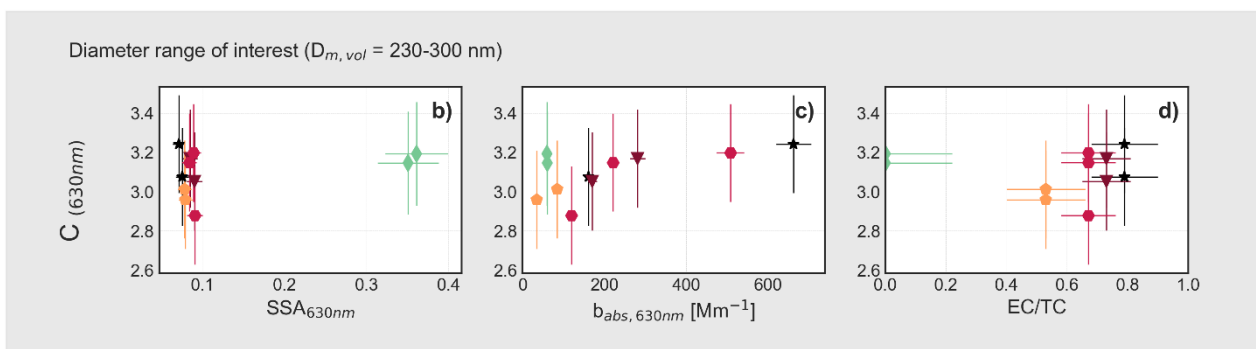
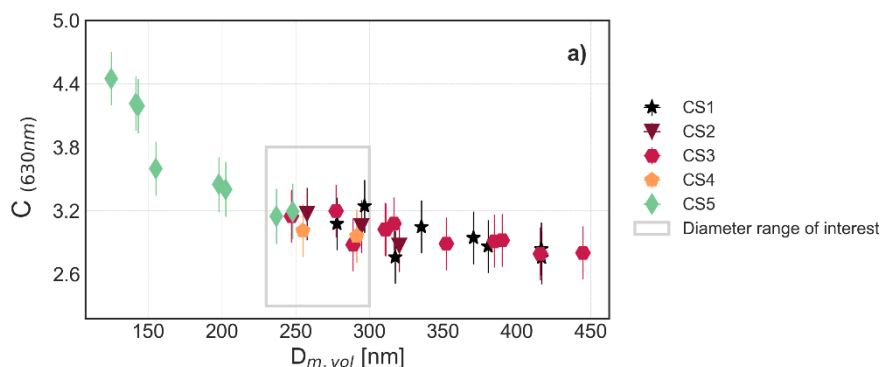
371

372 3.1.2 C dependence on soot microphysical properties: the dominating role of size

373 The C values at 630 nm averaged over each aethalometer filter spot interval were analyzed to identify the dependence on
374 average properties of the particles collected on the filter. These properties include particle size, absorption coefficient,
375 SSA, and chemical composition (measured as the EC/TC ratio). The results are summarized in Figure 1. ~~The analysis
376 shows that the C factor increases from 2.75 to 4.45 as the mean particle diameter of BC generated particles decreases
377 from 225.2 nm to 67.8 nm. This is particularly evident for particles smaller than 120 nm.~~ The analysis shows that the C
378 factor increases from 2.75 to 4.45 as the volume mean particle diameter of BC generated particles decreases from 444.8
379 nm to 124.9 nm. This is particularly evident for particles smaller than 200 nm, while at larger sizes the trend is not
380 significant when considering the associated uncertainties. The points with the highest C values and smallest sizes
381 correspond to experiments involving CS5 particles. These particles are not only smaller but also differ in composition,
382 with a negligible fraction of EC in spite of dominating OC composition. This compositional difference significantly
383 affects the optical properties, increasing the SSA from 0.05-0.09 for C1-CS4 to 0.27 for CS5 at 630 nm and the AAE
384 from around 1.27-1.88 to 3.79 (Heuser et al., 2025). However, focusing on a subset of points with limited size variability
385 (230-300 nm, highlighted in the grey box), it becomes evident that at similar diameters, C values are comparable for CS5
386 particles and CS1–CS4 particles. Moreover, for CS5 particles, C increases significantly from 3.15 to 4.45 as the volume
387 mean diameter decreases from 247.9 nm to 124.9 nm, while at larger sizes the trend is not significant when considering
388 the associated uncertainties. The points with the highest C values and smallest sizes correspond to experiments involving
389 CS5 particles. These particles are not only smaller but also differ in composition, with a negligible fraction of EC in spite
390 of dominating OC composition. This compositional difference significantly affects the optical properties, increasing the
391 SSA from 0.05-0.09 for C1-CS4 to 0.27 for CS5 at 630 nm and the AAE from around 1.27-1.88 to 3.79 (Heuser et al.,
392 2024). However, focusing on a subset of points with limited size variability (120-160 nm, highlighted in the grey box), it
393 becomes evident that at similar diameters, C values are comparable for CS5 particles and CS1–CS4 particles. Moreover,
394 for CS5 particles, C increases significantly from 3.15 to 4.45 as the mean diameter decreases from 132.9 nm to 67.8 nm.
395 This suggest that the size is the dominant factor impacting the C variability in these experiments. This result is likely
396 attributable to the greater penetration of smaller particles into the filter matrix (Huang et al., 2013; Hinds, 1999), that
397 affect the multiple scattering effects between particles and filter, leading to a larger overestimation of true absorption by
398 the aethalometer. This interpretation agrees with modelling results indicating that particle stratification increases the ratio
399 of filter-based and real absorption as particle size decreases (Moteki et al., 2010). Our results are consistent with previous
400 laboratory studies on other filter-based instruments such as COSMOS and PSAP (Lack et al., 2009; Nakayama et al.,
401 2010), and two previous studies on the aethalometer (Drinovec et al., 2022; Yus-Díez et al., 2025). These studies show
402 that for the AE33, C is larger for soot particles below ~250 nm than for particles above ~400 nm, while dust samples
403 generally exhibit lower C values, in line with reduced artefact for larger particles. This result is consistent with the impact
404 of particle size on absorption measurements in filter based instruments, as previously observed for the aethalometer
405 (Drinovec et al., 2022; Yus-Díez et al., 2025) and other instruments (Lack et al., 2009; Moteki et al., 2010; Nakayama et

406 al., 2010). Small particles, which can penetrate more deeply into the filter matrix and exhibit more isotropic scattering
 407 patterns, may enhance the multiple scattering effect, resulting in a greater overestimation of true absorption by the
 408 aethalometer.

409 The variability in SSA, which was observed to influence the C factor at high values in previous works (Yus-Díez et al.,
 410 2021), appears to have a limited impact in this low-SSA regime. The C-size dependence was observed for any loading
 411 correction scheme applied as shown in Supplementary Information.



412
 413 **Figure 1:** C dependence on particle size in laboratory studies measuring the properties of different freshly emitted particles (CS1–CS5).
 414 The top panel shows the C dependence on the size ($D_{m,geo}$). The bottom panels show the dependence of C values with the SSA, b_{abs}
 415 (measured by the EMS technique) and the EC/TC ratio, in experiments where the diameter was in the range 120–160 nm (grey rectangle
 416 in the top panel). C dependence on particle size in laboratory studies measuring the properties of different freshly emitted particles
 417 (CS1–CS5). The top panel shows the C dependence on the size ($D_{m,vol}$). The bottom panels show the dependence of C values with the
 418 SSA, b_{abs} (measured by the EMS technique) and the EC/TC ratio, in experiments where the diameter was in the range 230–300 nm
 419 (grey rectangle in the top panel).

420

421 3.2 Ambient variability of the C factor

422 In this section, the results obtained from field measurements on the environmental variability of the correction factor C
 423 are presented. These results provide insights into how C values fluctuate across different seasons and aerosol properties.

424 3.2.1 Average ambient C value and seasonal variability

425 The variability of the C factor at a wavelength of 637 nm was analysed on hourly base at the CMN site. The average C
 426 value over the period July 2020 - November 2022 is 2.35 with a standard deviation of 0.58. This value is comparable,
 427 within the combined uncertainties of MAAP and AE33 (27%), with the 2.45 value suggested by the ACTRIS guidelines
 428 for M8060 filter tape (obtained as the product of a C_{instr} factor (1.39) and the harmonization factor H^* (1.76);
 429 <https://www.actris-ecac.eu/particle-light-absorption.html>). This value is also in line, even if slightly lower, to mean values
 430 reported in other studies conducted at various sites (urban, background and mountain sites) using the same reference
 431 techniques (MAAP, MWAA) and filter tape, which range between 2.44 and 2.66 (Moschos et al., 2021; Valentini et al.,

2020; Yus-Díez et al., 2021). However, when considering the range of values reported in the literature, which consider different reference techniques for measuring absorption (e.g., two-wavelength Photothermal Aerosol Absorption Monitor PTAAM-2 λ , and the Cavity Attenuated Phase Shift CAPS SSA), various AE33 filter types, different wavelengths, and diverse environmental or experimental conditions (such as chamber studies with artificially generated soot or emissions from heavy fuel oil), the reported values can vary significantly from 2.26 to 8.26 (Corbin et al., 2018; Laing et al., 2020; Ferrero et al., 2021; Bernardoni et al., 2021; Kalbermatter et al., 2022). The averaged ambient value was also 23–66% lower compared to the average values obtained for freshly emitted soot in the chamber experiments. ~~This difference could be due to the use of different reference method for measuring absorption or it could reflect differences in particle composition.~~ The lower ambient values may be partly due to the different reference techniques used. The MAAP can exhibit a positive bias in absorption when compared with non-filter-based reference techniques as the EMS, particularly at relatively high SSA (>0.9), small particles (diameter <200 nm) and for aged aerosol (Yus-Díez et al., 2025; Kalbermatter et al., 2022; Romshoo et al., 2022). Such bias would lead to higher MAAP absorption values and, consequently, to lower C values in ambient measurements at CMN compared to those obtained in CESAM. In addition, the aethalometers operated at different flow rates in the ambient and chamber setups (5 and 2 L min⁻¹, respectively). As shown by Moteki et al. (2010) and Huang et al. (2013), variations in flow rate and face velocity can affect particle penetration and stratification by size within the filter. These effects may modify both the absolute value of C (which is expected to decrease with increasing flow rate) and its dependence on particle size. A detailed quantification of this effect is beyond the scope of the present study, but it may represent one of the factors contributing to the lower absolute C values observed in ambient measurements.

Figure 2 and Table 4 summarize the seasonal variability of C values at the CMN site. Throughout the year, C mean ranged from a minimum of 2.30 in spring to a maximum of 2.41 in winter, indicating a slight increase in the colder months. At the same time, the coldest seasons (winter and autumn), also showed the greatest variability, resulting in the highest standard deviations (0.7–0.8). The difference between the seasons, although significant based on the Kolmogorov-Smirnov test, was small compared to the combined instrumental uncertainty of the MAAP and the AE33.

Nonetheless, the seasonal variability observed at CMN was smaller in magnitude and opposite in trend compared to the biogenic-dominated site in the Finnish boreal forest (Luoma et al., 2021) and to the mountain site of Montsec d'Ares (Spain, 1570 m a.s.l.; Yus-Díez et al., 2021). In these previous studies, seasonal variability was explained as a result of dependence on optical (SSA; Yus-Díez et al., 2021) and microphysical (diameter; Luoma et al., 2021) properties, as well as aerosol composition (presence of dust; Yus-Díez et al., 2021). Hence, we addressed the dependency of C at CMN on particles properties, concentration and wavelength.

3.2.2 Lower limit of b_{abs} for C determination

One of the most critical challenges in determining C at a remote site like CMN, where aerosol concentrations are low, is that the absorption coefficient (b_{abs}) often approaches the detection limits of the instruments used. At very low concentrations, measurements are increasingly affected by instrumental noise, compromising the reliability of the resulting C values. To set a reasonable threshold for investigating the dependence of C on particle properties—while avoiding the exclusion of a substantial portion of the dataset—we first examined how C varies with the absorption coefficient (b_{abs}) measured with the MAAP, and assessed the influence of low b_{abs} values on the C estimates.

472 Figure 3 shows the dependence of C on b_{abs} , with higher C values observed at decreasing b_{abs} . In particular, C more
 473 frequently reaches values of 10 or higher when b_{abs} falls below 0.06 Mm^{-1} , although this condition accounts for less than
 474 3% of the dataset. These extreme values can significantly affect the median C (Figure 3), and are more commonly
 475 observed during winter and autumn (Table 4) seasons less influenced by anthropogenic emissions from the Po
 476 Valley (Marinoni et al., 2008). At such low b_{abs} levels—close to or below the detection limits of both the MAAP and
 477 AE33—the signal becomes increasingly dominated by instrumental noise, undermining the reliability of the computed C
 478 values (Cuesta-Mosquera et al., 2021). This likely explains both the higher standard deviation observed in winter and the
 479 unusually high C values recorded during that season. For this reason, data points where b_{abs} is below 0.06 Mm^{-1} were
 480 excluded from subsequent analyses.

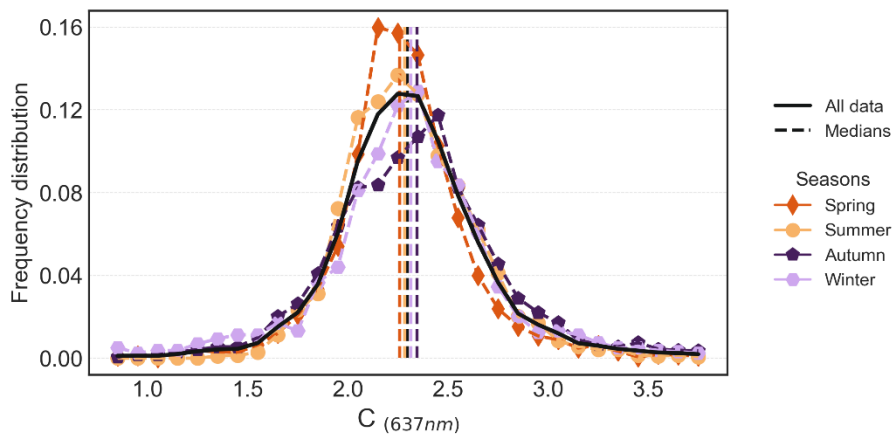
481

482 **Table 4:** The mean and standard deviation of C and b_{abs} for each season.

	Winter	Spring	Summer	Autumn	Whole
C					
Mean (SD)	2.40 (0.80)	2.30 (0.45)	2.32 (0.35)	2.41 (0.70)	2.35 (0.58)
b_{abs} [Mm^{-1}]					
Mean (SD)	0.77 (1.06)	1.49 (1.26)	1.89 (1.08)	1.08 (1.19)	1.36 (1.23)

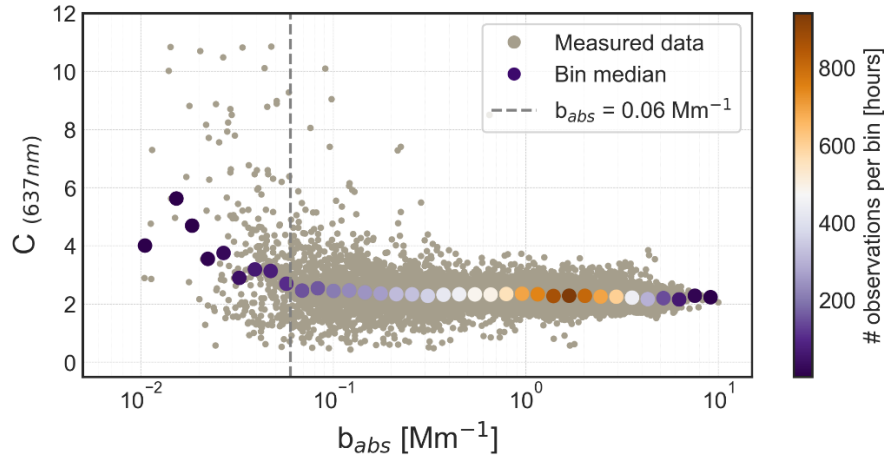
483

484



485

486 **Figure 2:** Histograms representing hourly averaged C values frequency distribution at 637 nm for the period July 2020 – November
 487 2022 at CMN. The black line represents the entire period, the coloured histograms correspond to each season in the analysed period.
 488 The median values corresponding to each season are also represented as dashed vertical lines. The MAAP was used as reference
 489 technique for measuring the absorption coefficient.



490

491 **Figure 3:** Scatterplot of hourly averaged C values at 637 nm as a function of the corresponding b_{abs} values measured [by the MAAP](#) at
 492 CMN. The reference technique used to measure the absorption coefficient is the MAAP. Bigger dots are used to represent the median
 493 C values in bins of b_{abs} .

494 3.2.3 C factor increase at high SSA

495 Previous studies have demonstrated that the optical properties of sampled particles can directly influence aethalometer
 496 measurements by altering the amount of scattered light, which the instrument may incorrectly interpret as absorption. An
 497 increase in the SSA has been linked in these studies to a corresponding rise in the C values (Schmid et al., 2006; Backman
 498 et al., 2017; Yus-Díez et al., 2021).

499

500 ~~During the period considered in this study, the SSA at 637 nm varied between 0.6 and 1. Here, the C values are binned to~~
 501 ~~the SSA values (Figure 4). The C values measured during the period considered in this study, are binned to the SSA~~
 502 ~~values (Figure 4).~~ The number of bins was chosen using the ‘auto’ mode of the numpy histogram_bin_edge function
 503 (python). This function selects as best number of bins, the highest value between those obtained with the Freedman and
 504 Diaconis, (1981) or the Sturges, (1926) criteria. For each bin, the median C and the corresponding 25th and 75th percentiles
 505 were derived.

506

507 At CMN, C remained relatively constant for SSA values below 0.90. It increased slowly for values between 0.90 and
 508 0.94, while a more significant variability was observed for SSA higher than 0.94 (Figure 4). This trend aligns with
 509 observations in other studies, where C becomes higher at higher SSA values due to an increase in the multiple scattering
 510 between particles and filter fibers and a reduced signal-to-noise ratio in low-absorption regimes (Schmid et al., 2006;
 511 Yus-Díez et al., 2021). The SSA-C relationship was fitted using the cross-sensitivity to scattering law proposed by Schmid
 512 et al. (2006) and applied in Yus-Díez et al. (2021) as:

513

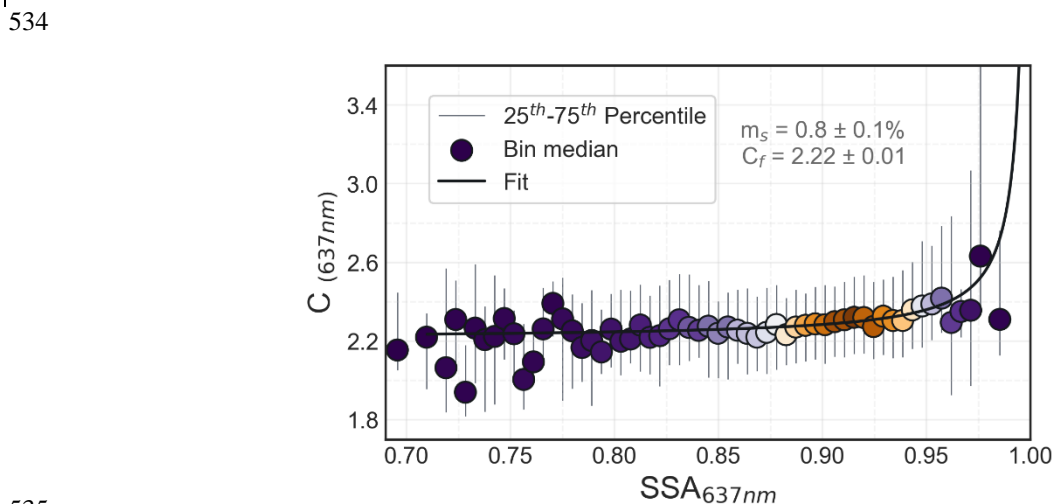
$$514 C = C_f + m_s \left(\frac{SSA}{1 - SSA} \right) \quad (7)$$

515

516 Compared to the results presented in Yus-Díez et al. (2021) for another mountaintop site, this curve shows a pronounced
 517 increase only at higher SSA values. The fitted curve closely matches the data up to a SSA of 0.97, becoming less
 518 representative at higher SSA. The deviation from the expected curve appears to be linked to the occurrence of strong dust
 519 events during the two-year period. In fact, over 80% of the hours with SSA values above 0.97 and C values below the
 520 mean of 2.3 correspond to days identified as dust-affected, characterized by coarse PM mass concentrations exceeding

521 37 $\mu\text{g}/\text{m}^3$, according to Vogel et al. (2025). The median C during these days is 2.0, suggesting a decrease in C during dust
 522 events, likely related to the increased presence of coarse particles collected on the filter, even at high SSA values. This
 523 decrease is consistent with the findings of Di Biagio et al. (2017), who reported lower C values for the AE31 when
 524 comparing measurements of ambient air and mineral dust particles.

525
 526 These results highlight the importance of carefully selecting appropriate correction factors. Under conditions of high SSA,
 527 absorption is typically minimal and may approach the detection limits of the instruments, increasing uncertainty in C
 528 estimation. ~~Moreover, part of the variability at high SSA values may arise from changes in aerosol properties, such as the~~
 529 ~~increased presence of coarse particles during dust events. Finally, the discrepancies observed in the fitted curves between~~
 530 ~~different sites, underscore the complexity and site specific nature of C behaviour, particularly under clean or dust-~~
 531 ~~influenced conditions. Moreover, we should consider that this dependence, estimated using the MAAP as a reference,~~
 532 ~~may have been underestimated. As shown by Yus-Díez et al. (2025), this instrument is also affected by cross-sensitivity~~
 533 ~~to scattering when compared with a non-filter-based technique.~~



535
 536 **Figure 4:** C (637 nm) dependence on the SSA (derived at 637 nm combining MAAP and nephelometer). Reference absorption
 537 instrument: MAAP. Dots represent the mean values in each SSA bin, the gray lines the 25th and 75th percentile. The dots colours
 538 represent the number of observations used in each bin for calculating the mean and the curve obtained using Yus-Díez et al. (2021)
 539 relation.

540
 541

542 3.2.4 C factor increase with decreasing particles size

543 ~~Previous studies have suggested a possible influence of particle size on the C value (Bernardoni et al., 2021, Luoma et~~
 544 ~~al., 2021, Drinovec et al., 2022; Yus-Díez et al., 2025). A clear relationship between C and the size of freshly generated~~
 545 ~~soot, has also been observed in this study through chamber experiments. In this section, we investigate how C at 637 nm~~
 546 ~~varies with particle size under ambient atmospheric conditions, where isolating the effect of a specific property is more~~
 547 ~~challenging. The aim is to assess whether particle size continues to play a significant role in such complex environments.~~

548
 549 ~~During the period studied at CMN, the hourly geometric mean diameter ($D_{m,geo}$) of total aerosol particles ranged from 19~~
 550 ~~to 173 nm. The analysis of C as a function of particle size revealed a slight (within 15%) C increase as $D_{m,geo}$ decreases~~
 551 ~~(Figure 5), not only observed in the median C values but also for the 25th and 75th percentiles. This analysis was performed~~

552 ~~by binning C values by particle size ($D_{m,geo}$) and then calculating the median and percentiles in each bin, using the same~~
553 ~~approach applied for the SSA.~~

554 In this section, we examine the dependence of the C factor on particle size under ambient atmospheric conditions, where
555 isolating the influence of individual aerosol properties is not straightforward. The objective is to evaluate whether particle
556 size remains a significant driver of C variability. The analysis was performed by binning C values according to the aerosol
557 volume mean diameter and computing the median together with the 25th and 75th percentiles within each bin, following
558 the same procedure adopted for SSA.

559 During the observation period at CMN, the hourly $D_{m,vol}$ of total aerosol particles ranged from 134.5 nm to 738.9 nm. The
560 resulting C–size relationship shows an increase of approximately 25% in C as $D_{m,vol}$ decreases from 732.1 nm to 141.4
561 nm (Figure 5). This trend is consistently observed across the median as well as the interquartile range, indicating a clear
562 dependence of C on particle size.

563 To ensure that the observed variability in C was not primarily driven by other parameters—such as the SSA or
564 exceptionally low absorption values—rather than by particle size itself, we examined the mean SSA and absorption
565 coefficient within each size bin. The results show that neither of these parameters alone can account for the whole
566 observed variability in C with size in Figure 5 (see Supplementary Information, Figure S3 and Figure S4).

567 Although its influence is moderate compared to the instrumental uncertainty, particle size appears to affect C even under
568 ambient atmospheric conditions. This suggests that variations in particle size could contribute to the differences in C
569 observed across sites and seasons, as proposed in previous studies (Bernardoni et al., 2021; Luoma et al., 2021),
570 particularly when there are significant changes in the mean volume size distribution or during specific events. At CMN,
571 this effect can be especially significant during dust transport events, which occur on about 20% of days throughout the
572 year (Vogel et al., 2025). As shown in Supplementary Information Figure S7, C at 637 nm decreases with increasing dust
573 event intensity, consistently with the findings of Yus-Díez et al., (2025).

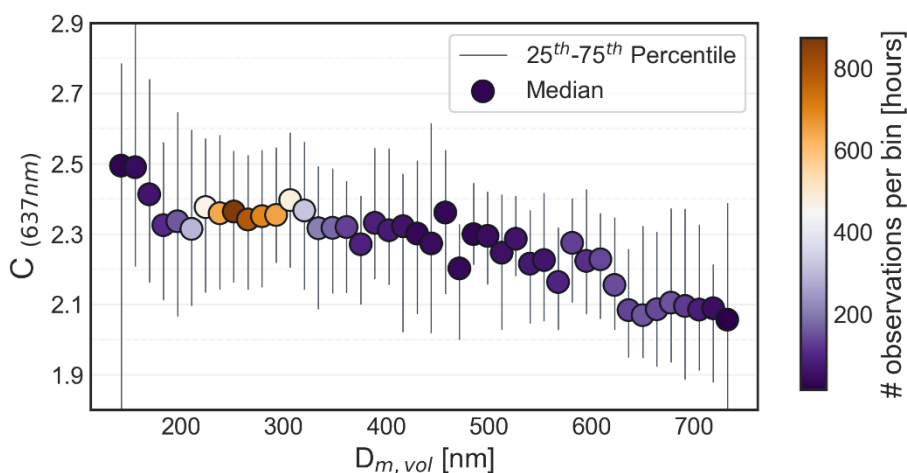
574 When comparing the size dependence of C with that observed in the chamber experiments and in other laboratory studies
575 on soot (Drinovec et al., 2022; Yus-Díez et al., 2025), the ambient relationship appears more linear and overall weaker.
576 This attenuation may be partly related to the use of the MAAP. Its positive bias compared to non filter-based techniques
577 could be more relevant for smaller particles (Moteki et al., 2010; Romshoo et al., 2022). As a result, the influence of
578 particle size on C under ambient conditions could be partially masked by the measurement bias inherent to the reference
579 technique used. Differences in sampling flow of the aethalometer between the ambient and chamber measurements may
580 also have contributed to this weaker dependence, since different flow rates are expected to affect the penetration of the
581 particles as well as the resulting C dependence on size (Moteki et al., 2010; Huang et al., 2013).

582
583 ~~This trend is in line with the results obtained from chamber experiments and previous studies (Nakayama et al., 2010;~~
584 ~~Drinovec et al., 2022; Yus-Díez et al., 2025), but small compared to the instrumental uncertainties. However, it could~~
585 ~~cause more significant bias in the individual hourly values and actually be one of the causes of the observed variability~~
586 ~~of C at different sites and seasons.~~

587

588 Moreover, the C increase is less pronounced than what was observed in chamber experiments (over 60%). This difference
 589 may be due to the distinct properties of the particles studied—only absorbing in the chamber and mixed in ambient air—
 590 as well as differences in reference measurement techniques. The MAAP, being a filter-based instrument, may be affected
 591 as well by particle stratification, making its radiative transfer model an approximation potentially biased, as discussed by
 592 Moteki et al. (2010).

593
 594



595

596 **Figure 5:** C (637 nm) dependence on the geometric mean diameter $D_{m,geo}$. Reference absorption instrument: MAAP. Dots represent
 597 the mean values in each $D_{m,geo}$ bin, the gray lines the 25th and 75th percentile. The dots colours represent the number of observations
 598 used in each bin for calculating the median. C (637 nm) dependence on the geometric mean diameter $D_{m,vol}$. Reference absorption
 599 instrument: MAAP. Dots represent the mean values in each $D_{m,vol}$ bin, the gray lines the 25th and 75th percentile. The dots colours
 600 represent the number of observations used in each bin for calculating the median.

601

602 3.2.5 Absence of spectral dependence

603 Figure 6 shows the spectral dependence of C at CMN for observations between September and October 2022, with 43
 604 filters collected. The mean C values range from 2.38 ± 0.62 at 470 nm to 2.13 ± 0.60 at 880 nm (Table 5 Table 5). A
 605 statistical Kolmogorov-Smirnov test was applied to quantify the significance of the spectral dependence, and a potentially
 606 significant distinction was observed between the 470 nm and 880 nm mean C values (p -value = 0.042). However, for all
 607 other wavelength pairs, the test yielded $p > 0.05$, indicating no statistically significant differences, and that despite the
 608 high variability in the data, with standard deviations reaching 0.63. Since the overall precision of the AE33 is not
 609 wavelength-dependent (Cuesta-Mosquera et al., 2021), all wavelength-dependent C values reported in this study fall
 610 within the relative error of $\pm 31\%$, obtained combining the AE33 and MWAA uncertainties.

611

612 Limited studies have investigated the multi-wavelength absorption reference methods for both models of the
 613 aethalometer. For the AE31 model, Bernardoni et al. (2021) and Ferrero et al. (2021) did not observe a notable wavelength
 614 dependence of the C factor, although they found that applying a wavelength-dependent C correction improved the
 615 agreement in the measured absorption coefficient for both AE31 and AE33. In contrast, for the AE33 model, neither
 616 Bernardoni et al. (2021) nor Ferrero et al. (2021) detected significant wavelength dependence after accounting for
 617 uncertainties. However, Moschos et al. (2021) reported a decreasing trend in the C factor from 2.5 at 370 nm to 2.3 at 880
 618 nm in Swiss background conditions. Moreover, Yus-Díez et al. (2021) found no significant wavelength dependence,
 619 except for aged aerosols, where they observed an increasing C value with wavelength, ranging from 3.47 to 4.03.

620

621

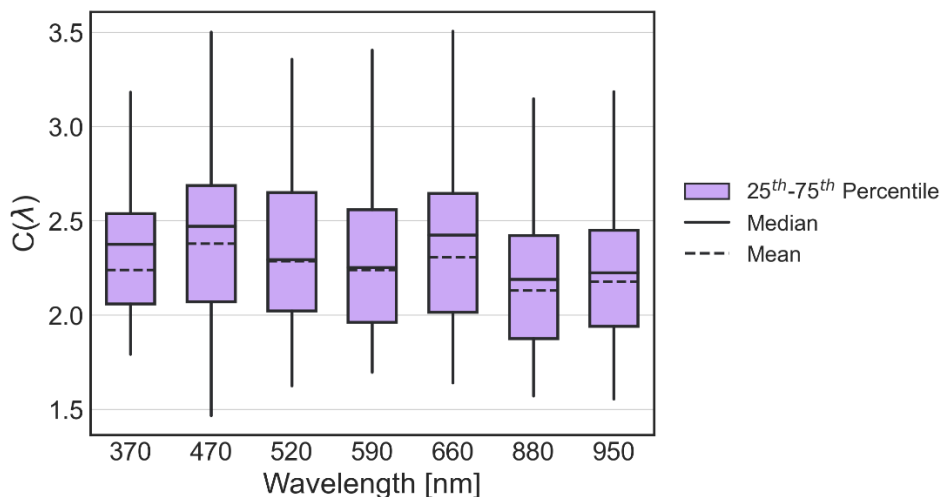
622

Table 5: Mean and standard deviation (SD) of C values for each aethalometer wavelength at CMN. The MWAA was used as reference instrument for the absorption coefficient.

	370 nm	470 nm	520 nm	590 nm	660 nm	880 nm	950 nm
Mean	2.24	2.38	2.29	2.24	2.31	2.13	2.18
(SD)	(0.58)	(0.62)	(0.58)	(0.58)	(0.63)	(0.60)	(0.63)

623

624



625

626

627

Figure 6: Boxplots describing the statistics of C values derived at each aethalometer wavelength, the 25th – 75th percentile range (IQR), the mean and median are reported. The MWAA was used as the reference technique for measuring the absorption coefficient.

628

629 4 Conclusions

630 In this work we studied the role of aerosol properties on the variability of the multiple scattering correction factor C for
 631 the dual-spot aethalometer AE33. For this, we combined data from a long term series in a mountaintop station in northern
 632 Italy at Monte Cimone, CMN, and from multiple experiments on laboratory-generated soot at the CESAM simulation
 633 chamber. We calculated the C factor comparing the attenuation coefficient measured by the AE33 with the absorption
 634 coefficient measured with independent techniques: the MAAP and MWAA at CMN, and the extinction-minus-scattering
 635 in chamber experiments.

636

637 The C factor obtained by chamber experiments ranged from 2.89 to 3.9 at 630 nm, the highest values corresponding to
 638 higher organic content and smaller particle sizes, while the lowest values corresponding to a higher content of elemental
 639 carbon and larger particle sizes. The possible dependence of the retrieved C on the loading correction scheme applied was
 640 also evaluated and quantified in max 30% of difference in the averaged values.

641

642 We found an averaged C factor at 637 nm of 2.35 ± 0.58 at CMN. This value shows a slight seasonal variability with
 643 higher values in winter than in summer, difficult to associate to specific particle properties and mainly driven by the
 644 impact on C of the very low signal-to-noise ratio of the absorption coefficient, causing very high C values at low b_{abs}
 645 ($<0.06 \text{ Mm}^{-1}$). This was significant particularly at very high SSA values (>0.94), where an impact of the low signal-to-
 646 noise ratio of the absorption coefficient cannot be excluded. Moreover, part of the variability at high SSA values was

647 influenced by changes in aerosol properties, such as the increased presence of coarse particles during dust events. We
648 studied also the C spectral dependence finding no evidence of a variability of C within the 370-950 nm spectral range.

649

650 ~~The present analysis evidences a dependence of C to particle size. This dependence was small (within 15%) in ambient
651 conditions for mostly scattering aerosols, while it was more pronounced (>60%) in chamber experiments measuring only
652 soot particles and using a non-filter based technique as reference for the absorption coefficient. This dependence observed
653 previously for filter based instruments could explain part of the C factor variability in literature and should be investigated
654 deeply to improve the accuracy of absorption coefficient measurements in international research infrastructures.~~

655 The present analysis evidences a dependence of C on particle size. This dependence was moderate (within 25%) under
656 ambient conditions dominated by mostly scattering aerosols, while it became much more pronounced (>60%) in chamber
657 experiments using soot-only particles and a non-filter-based absorption reference. This behaviour likely contributes to
658 the variability of C values reported in the literature and highlights the need for further investigation to improve the
659 accuracy of absorption coefficient measurements within international research infrastructures.

660 The consistency between chamber and ambient results indicates that, although the chamber setup better isolates the size
661 dependence, this effect is also detectable under complex real-world aerosol conditions. These findings suggest that C may
662 vary systematically across monitoring sites depending on the dominant particle size modes—for example, smaller C
663 values at sites dominated by larger, aged particles, and higher C values at locations influenced by fresh combustion or
664 nucleation events. Further studies, combining targeted chamber experiments and modelling under a wider range of
665 conditions, are needed to better quantify these dependencies and support the development of more generalizable
666 parameterizations for harmonized absorption measurements and improved data quality in monitoring networks.

667 5 Appendix

668 **Table A1.** List of digital object identifier (DOI) for the CESAM chamber experimental data supporting the findings of this study.
669 Those data are available through the Database of Atmospheric Simulation Chamber Studies (DASCS) of the EUROCHAMP Data
670 Centre (<https://data.eurochamp.org/data-access/chamber-experiments/>).

671

Cast Soot Type (Date of experiment)	Dataset DOI reference in the EUROCHAMP Data Centre
CS1 (23/02/2021)	https://doi.org/10.25326/8KVR-AA70
CS1 (24/02/2021)	https://doi.org/10.25326/M24W-V933
CS1 (19/10/2021)	https://doi.org/10.25326/5144-DY86
CS1 (12/12/2022)	https://doi.org/10.25326/2BD3-Q151
CS1 (14/12/2022)	https://doi.org/10.25326/9G66-MG61
CS1 (15/12/2022)	https://doi.org/10.25326/XJKP-JD08
CS1 (16/12/2022)	https://doi.org/10.25326/6030-BD74
CS2 (20/10/2021)	https://doi.org/10.25326/ET9M-7H20
CS3 (26/10/2021)	https://doi.org/10.25326/0HMW-HM76
CS3 (06/12/2022)	https://doi.org/10.25326/T145-0S52
CS3 (07/12/2022)	https://doi.org/10.25326/9TR7-BB18
CS4 (22/10/2021)	https://doi.org/10.25326/VPM3-3W86
CS5 (28/05/2021)	https://doi.org/10.25326/BGCT-4J45
CS5 (21/10/2021)	https://doi.org/10.25326/34DX-YJ98
CS5 (08/12/2022)	https://doi.org/10.25326/FWN3-A342
CS5 (09/12/2022)	https://doi.org/10.25326/6M6N-8P33

672

673 **6 Open Research / Data availability**

674 The CESAM data used in this study are available through the Database of Atmospheric Simulation Chamber Studies
675 (DASCS) of the EUROCHAMP Data Centre (<https://data.eurochamp.org/data-access/chamber-experiments/>) with the
676 identifiers listed in Appendix Table A1. The CMN database is available through ACTRIS DC (EBAS/NILU) and [dust
677 event identification at CMN is available through the ITINERIS HUB \(https://doi.org/10.71763/XDZA-FA77\)](https://doi.org/10.71763/XDZA-FA77).

678 **7 Competing interests**

679 The authors declare that they have no competing interests.

680 **8 Author contributions**

681 LR, AM and CDB conceived the study and discussed the results. LR, AM, MM took care of field measurements. JH and
682 LR conducted the CESAM experiments with contributions by CDB, MC, AB, EP, AM, JY, CY, MZ, PF, BPV, and JFD.
683 DM, TI and VV performed the MWAA measurements. LR performed the full data analysis under the supervision of MZ,
684 AM and CDB and with contributions from JH, ~~and~~ MM and FV. CDB contributed to funding acquisition and project
685 administration for CESAM experiments. LR, MZ, AM and CDB wrote the manuscript. All authors reviewed and
686 commented on the paper.

687 **9 Acknowledgements**

688 The CNRS-INSU is gratefully acknowledged for supporting the CESAM chamber as a national facility included in the
689 ACTRIS-France Research Infrastructure as well as AERIS (<https://www.aeris-data.fr/>) for curing and distributing the data
690 through the EUROCHAMP Data Center (<https://data.eurochamp.org/>). We thank ACTRIS-Italy for supporting
691 measurements at Monte Cimone, carried out within ACTRIS Research infrastructure (ESFRI).

692 **10 Funding**

693 This work has received funding from the TNA activity of the European Union's Horizon 2020 research and innovation
694 programme through the EUROCHAMP-2020 Infrastructure Activity under grant agreement No 730997. This study has
695 been supported by the French National Research Agency (ANR) through the B2C project (contract ANR-19-CE01-0024-
696 01), by the French National program LEFE-CHAT (Les Enveloppes Fluides et l'Environnement – Chimie
697 Atmosphérique) through the BACON project. It has been also supported by DIM Qi² and Paris Ile-de-France Region. L.
698 Renzi and M. Zanatta were partially supported by ITINERIS project (IR0000032), the Italian Integrated Environmental
699 Research Infrastructures System (D.D. n. 130/2022 - CUP B53C22002150006) Funded by EU - Next Generation EU
700 PNRR- Mission 4 "Education and Research". The measurements at Monte Cimone were carried out within ACTRIS RI
701 and supported by the Italian Ministry project PER_ACTRIS_IT, under PNIR (Piano Nazionale Infrastrutture di Ricerca)
702 2014 – 2020.

703 **11 References:**

- 704 Anderson, T. L. and Ogren, J. A.: Determining Aerosol Radiative Properties Using the TSI 3563 Integrating
705 Nephelometer, *Aerosol Science and Technology*, 29, 57–69, <https://doi.org/10.1080/02786829808965551>, 1998.
- 706 Anderson, T. L., Covert, D. S., Marshall, S. F., Laucks, M. L., Charlson, R. J., Waggoner, A. P., Ogren, J. A., Caldwell,
707 R., Holm, R. L., Quant, F. R., Sem, G. J., Wiedensohler, A., Ahlquist, N. A., and Bates, T. S.: Performance Characteristics
708 of a High-Sensitivity, Three-Wavelength, Total Scatter/Backscatter Nephelometer, *Journal of Atmospheric and Oceanic*
709 *Technology*, 13, 967–986, [https://doi.org/10.1175/1520-0426\(1996\)013<0967:PCOAHS>2.0.CO;2](https://doi.org/10.1175/1520-0426(1996)013<0967:PCOAHS>2.0.CO;2), 1996.
- 710 Andrews, E., Ogren, J. A., Bonasoni, P., Marinoni, A., Cuevas, E., Rodríguez, S., Sun, J. Y., Jaffe, D. A., Fischer, E. V.,
711 Baltensperger, U., Weingartner, E., Coen, M. C., Sharma, S., Macdonald, A. M., Leaitch, W. R., Lin, N.-H., Laj, P.,
712 Arsov, T., Kalapov, I., Jefferson, A., and Sheridan, P.: Climatology of aerosol radiative properties in the free troposphere,
713 *Atmospheric Research*, 102, 365–393, <https://doi.org/10.1016/j.atmosres.2011.08.017>, 2011.
- 714 Arnott, W. P., Hamasha, K., Moosmüller, H., Sheridan, P. J., and Ogren, J. A.: Towards aerosol light-absorption
715 measurements with a 7-wavelength aethalometer: Evaluation with a photoacoustic instrument and 3-wavelength
716 nephelometer, *Aerosol Science and Technology*, 39, 17–29, <https://doi.org/10.1080/027868290901972>, 2005.
- 717 Backman, J., Schmeisser, L., Virkkula, A., Ogren, J. A., Asmi, E., Starkweather, S., Sharma, S., Eleftheriadis, K., Uttal,
718 T., Jefferson, A., Bergin, M., Makshtas, A., Tunved, P., and Fiebig, M.: On Aethalometer measurement uncertainties and
719 an instrument correction factor for the Arctic, *Atmospheric Measurement Techniques*, 10, 5039–5062,
720 <https://doi.org/10.5194/amt-10-5039-2017>, 2017.
- 721 Baldo, C., Formenti, P., Di Biagio, C., Lu, G., Song, C., Cazaunau, M., Pangui, E., Doussin, J.-F., Dagsson-
722 Waldhauserova, P., Arnalds, O., Beddows, D., MacKenzie, A. R., and Shi, Z.: Complex refractive index and single
723 scattering albedo of Icelandic dust in the shortwave spectrum, *Aerosols/Laboratory Studies/Troposphere/Physics*
724 (physical properties and processes), <https://doi.org/10.5194/egusphere-2023-276>, 2023.
- 725 Bernardoni, V., Ferrero, L., Bolzacchini, E., Forello, A. C., Gregorič, A., Massabò, D., Močnik, G., Prati, P., Rigler, M.,
726 Santagostini, L., Soldan, F., Valentini, S., Valli, G., and Vecchi, R.: Determination of Aethalometer multiple-scattering
727 enhancement parameters and impact on source apportionment during the winter 2017/18 EMEP/ACTRIS/COLOSSAL
728 campaign in Milan, *Atmospheric Measurement Techniques*, 14, 2919–2940, <https://doi.org/10.5194/amt-14-2919-2021>,
729 2021.
- 730 Berry, G., Beckman, I., and Cho, H.: A comprehensive review of particle loading models of fibrous air filters, *Journal of*
731 *Aerosol Science*, 167, 106078, <https://doi.org/10.1016/j.jaerosci.2022.106078>, 2023.
- 732 Bescond, A., Yon, J., Ouf, F.-X., Rozé, C., Coppalle, A., Parent, P., Ferry, D., and Laffon, C.: Soot optical properties
733 determined by analyzing extinction spectra in the visible near-UV: Toward an optical speciation according to constituents
734 and structure, *Journal of Aerosol Science*, 101, 118–132, <https://doi.org/10.1016/j.jaerosci.2016.08.001>, 2016.
- 735 Bond, T. C., Doherty, S. J., Fahey, D. W., Forster, P. M., Berntsen, T., DeAngelo, B. J., Flanner, M. G., Ghan, S., Kärcher,
736 B., Koch, D., Kinne, S., Kondo, Y., Quinn, P. K., Sarofim, M. C., Schultz, M. G., Schulz, M., Venkataraman, C., Zhang,
737 H., Zhang, S., Bellouin, N., Guttikunda, S. K., Hopke, P. K., Jacobson, M. Z., Kaiser, J. W., Klimont, Z., Lohmann, U.,
738 Schwarz, J. P., Shindell, D., Storelvmo, T., Warren, S. G., and Zender, C. S.: Bounding the role of black carbon in the
739 climate system: A scientific assessment, *Journal of Geophysical Research: Atmospheres*, 118, 5380–5552,
740 <https://doi.org/10.1002/jgrd.50171>, 2013.
- 741 Brégonzio-Rozier, L., Giorio, C., Siekmann, F., Pangui, E., Morales, S. B., Temime-Roussel, B., Gratien, A., Michoud,
742 V., Cazaunau, M., DeWitt, H. L., Tapparo, A., Monod, A., and Doussin, J.-F.: Secondary organic aerosol formation from
743 isoprene photooxidation during cloud condensation–evaporation cycles, *Atmospheric Chemistry and Physics*, 16, 1747–
744 1760, <https://doi.org/10.5194/acp-16-1747-2016>, 2016.
- 745 Caponi, L., Formenti, P., Massabó, D., Di Biagio, C., Cazaunau, M., Pangui, E., Chevaillier, S., Landrot, G., Andreae,
746 M. O., Kandler, K., Piketh, S., Saeed, T., Seibert, D., Williams, E., Balkanski, Y., Prati, P., and Doussin, J.-F.: Spectral-
747 and size-resolved mass absorption efficiency of mineral dust aerosols in the shortwave spectrum: a simulation chamber
748 study, *Atmospheric Chemistry and Physics*, 17, 7175–7191, <https://doi.org/10.5194/acp-17-7175-2017>, 2017.

- 749 Chung, C. E., Ramanathan, V., and Decremer, D.: Observationally constrained estimates of carbonaceous aerosol
750 radiative forcing, *Proceedings of the National Academy of Sciences*, 109, 11624–11629,
751 <https://doi.org/10.1073/pnas.1203707109>, 2012.
- 752 Collaud Coen, M., Weingartner, E., Apituley, A., Ceburnis, D., Fierz-Schmidhauser, R., Flentje, H., Henzing, J. S.,
753 Jennings, S. G., Moerman, M., Petzold, A., Schmid, O., and Baltensperger, U.: Minimizing light absorption measurement
754 artifacts of the Aethalometer: evaluation of five correction algorithms, *Atmospheric Measurement Techniques*, 3, 457–
755 474, <https://doi.org/10.5194/amt-3-457-2010>, 2010.
- 756 Corbin, J. C., Pieber, S. M., Czech, H., Zanatta, M., Jakobi, G., Massabò, D., Orasche, J., El Haddad, I., Mensah, A. A.,
757 Stengel, B., Drinovec, L., Mocnik, G., Zimmermann, R., Prévôt, A. S. H., and Gysel, M.: Brown and Black Carbon
758 Emitted by a Marine Engine Operated on Heavy Fuel Oil and Distillate Fuels: Optical Properties, Size Distributions, and
759 Emission Factors, *Journal of Geophysical Research: Atmospheres*, 123, 6175–6195,
760 <https://doi.org/10.1029/2017JD027818>, 2018.
- 761 Cristofanelli, P., Marinoni, A., Arduini, J., Bonafè, U., Calzolari, F., Colombo, T., Decesari, S., Duchi, R., Facchini, M.
762 C., Fierli, F., Finessi, E., Maione, M., Chiari, M., Calzolari, G., Messina, P., Orlandi, E., Roccato, F., and Bonasoni, P.:
763 Significant variations of trace gas composition and aerosol properties at Mt. Cimone during air mass transport from North
764 Africa – contributions from wildfire emissions and mineral dust, *Atmospheric Chemistry and Physics*, 9, 4603–
765 4619, <https://doi.org/10.5194/acp-9-4603-2009>, 2009.
- 766 Cristofanelli, P., Brattich, E., Decesari, S., Landi, T. C., Maione, M., Putero, D., Tositti, L., and Bonasoni, P.: The “O.
767 Vittori” Observatory at Mt. Cimone: A “Lighthouse” for the Mediterranean Troposphere, in: *High-Mountain Atmospheric
768 Research : The Italian Mt. Cimone WMO/GAW Global Station (2165 m a.s.l.)*, edited by: Cristofanelli, P., Brattich, E.,
769 Decesari, S., Landi, T. C., Maione, M., Putero, D., Tositti, L., and Bonasoni, P., Springer International Publishing, Cham,
770 1–14, https://doi.org/10.1007/978-3-319-61127-3_1, 2018.
- 771 Cristofanelli, P., Trisolino, P., Calzolari, F., Busetto, M., Calidonna, C. R., Amendola, S., Arduini, J., Fratticioli, C.,
772 Hundal, R. A., Maione, M., Marcucci, F., Marinoni, A., Montaguti, S., Renzi, L., Roccato, F., Bonasoni, P., and Putero,
773 D.: Influence of wildfire emissions to carbon dioxide (CO₂) observed at the Mt. Cimone station (Italy, 2165 m asl): A
774 multi-year investigation, *Atmospheric Environment*, 330, 120577, <https://doi.org/10.1016/j.atmosenv.2024.120577>,
775 2024.
- 776 Cuesta-Mosquera, A., Močnik, G., Drinovec, L., Müller, T., Pfeifer, S., Minguillón, M. C., Briel, B., Buckley, P.,
777 Dudoitis, V., Fernández-García, J., Fernández-Amado, M., Ferreira De Brito, J., Riffault, V., Flentje, H., Heffernan, E.,
778 Kalivitis, N., Kalogridis, A.-C., Keernik, H., Marmureanu, L., Luoma, K., Marinoni, A., Pikridas, M., Schauer, G.,
779 Serfozo, N., Servomaa, H., Titos, G., Yus-Díez, J., Ziola, N., and Wiedensohler, A.: Intercomparison and characterization
780 of 23 Aethalometers under laboratory and ambient air conditions: procedures and unit-to-unit variabilities, *Atmospheric
781 Measurement Techniques*, 14, 3195–3216, <https://doi.org/10.5194/amt-14-3195-2021>, 2021.
- 782 De Haan, D. O., Hawkins, L. N., Jansen, K., Welsh, H. G., Pednekar, R., de Loera, A., Jimenez, N. G., Tolbert, M. A.,
783 Cazaunau, M., Gratien, A., Bergé, A., Pangui, E., Formenti, P., and Doussin, J.-F.: Glyoxal’s impact on dry ammonium
784 salts: fast and reversible surface aerosol browning, *Atmospheric Chemistry and Physics*, 20, 9581–9590,
785 <https://doi.org/10.5194/acp-20-9581-2020>, 2020.
- 786 Denjean, C., Formenti, P., Picquet-Varrault, B., Camredon, M., Pangui, E., Zapf, P., Katrib, Y., Giorio, C., Tapparo, A.,
787 Temime-Roussel, B., Monod, A., Aumont, B., and Doussin, J. F.: Aging of secondary organic aerosol generated from the
788 ozonolysis of α -pinene: effects of ozone, light and temperature, *Atmospheric Chemistry and Physics*, 15, 883–897,
789 <https://doi.org/10.5194/acp-15-883-2015>, 2015.
- 790 Di Biagio, C., Formenti, P., Doppler, L., Gaimoz, C., Grand, N., Ancellet, G., Attié, J.-L., Bucci, S., Dubuisson, P., Fierli,
791 F., Mallet, M., and Ravetta, F.: Continental pollution in the Western Mediterranean basin: large variability of the aerosol
792 single scattering albedo and influence on the direct shortwave radiative effect, *Atmos. Chem. Phys.*, 16, 10591–10607,
793 <https://doi.org/10.5194/acp-16-10591-2016>, 2016.
- 794 Di Biagio, C., Formenti, P., Cazaunau, M., Pangui, E., Marchand, N., and Doussin, J.-F.: Aethalometer multiple scattering
795 correction C_{ref} for mineral dust aerosols, *Atmospheric Measurement Techniques*, 10, 2923–2939,
796 <https://doi.org/10.5194/amt-10-2923-2017>, 2017.
- 797 Di Biagio, C., Formenti, P., Balkanski, Y., Caponi, L., Cazaunau, M., Pangui, E., Journet, E., Nowak, S., Andreae, M.
798 O., Kandler, K., Saeed, T., Piketh, S., Seibert, D., Williams, E., and Doussin, J.-F.: Complex refractive indices and single-

799 scattering albedo of global dust aerosols in the shortwave spectrum and relationship to size and iron content, *Atmospheric*
800 *Chemistry and Physics*, 19, 15503–15531, <https://doi.org/10.5194/acp-19-15503-2019>, 2019.

801 Drinovec, L., Močnik, G., Zotter, P., Prévôt, A. S. H., Ruckstuhl, C., Coz, E., Rupakheti, M., Sciare, J., Müller, T.,
802 Wiedensohler, A., and Hansen, A. D. A.: The “dual-spot” Aethalometer: an improved measurement of aerosol black
803 carbon with real-time loading compensation, *Atmospheric Measurement Techniques*, 8, 1965–1979,
804 <https://doi.org/10.5194/amt-8-1965-2015>, 2015.

805 Drinovec, L., Jagodič, U., Pirker, L., Škarabot, M., Kurtjak, M., Vidović, K., Ferrero, L., Visser, B., Röhrbein, J.,
806 Weingartner, E., Kalbermatter, D. M., Vasilatou, K., Bühlmann, T., Pascale, C., Müller, T., Wiedensohler, A., and
807 Močnik, G.: A dual-wavelength photothermal aerosol absorption monitor: design, calibration and performance,
808 *Atmospheric Measurement Techniques*, 15, 3805–3825, <https://doi.org/10.5194/amt-15-3805-2022>, 2022.

809 [Duchi, R., Cristofanelli, P., Landi, T. C., Arduini, J., Bonafè, U., Bourcier, L., Busetto, M., Calzolari, F., Marinoni, A.,](https://doi.org/10.12952/journal.elementa.000085)
810 [Putero, D., and Bonasoni, P.: Long-term \(2002–2012\) investigation of Saharan dust transport events at Mt. Cimone GAW](https://doi.org/10.12952/journal.elementa.000085)
811 [global station, Italy \(2165 m 360 a.s.l.\), 4, 000 085, https://doi.org/10.12952/journal.elementa.000085, 2016.](https://doi.org/10.12952/journal.elementa.000085)

812 Favez, O., Weber, S., Petit, J.-E., Alleman, L., Albinet, A., Riffault, V., Chazeau, B., Amodeo, T., Salameh, D., Zhang,
813 Y., Srivastava, D., Samaké, A., Aujay-Plouzeau, R., Papin, A., Bonnaire, N., Boullanger, C., Chatain, M., Chevrier, F.,
814 Detournay, A., Dominik-Sègue, M., Falhun, R., Garbin, C., Gherzi, V., Grignon, G., Levigoureux, G., Pontet, S.,
815 Rangognio, J., Zhang, S., Besombes, J.-L., Conil, S., Uzu, G., Savarino, J. E., Marchand, N., Gros, V., Marchand, C.,
816 Jaffrezo, J.-L., and Leoz-Garziandia, E.: Overview of the French Operational Network for In Situ Observation of PM
817 Chemical Composition and Sources in Urban Environments (CARA Program), *Atmosphere*, 12, 207,
818 <https://doi.org/10.3390/atmos12020207>, 2021.

819 Ferrero, L., Bernardoni, V., Santagostini, L., Cogliati, S., Soldan, F., Valentini, S., Massabò, D., Močnik, G., Gregorič,
820 A., Rigler, M., Prati, P., Bigogno, A., Losi, N., Valli, G., Vecchi, R., and Bolzacchini, E.: Consistent determination of the
821 heating rate of light-absorbing aerosol using wavelength- and time-dependent Aethalometer multiple-scattering
822 correction, *Science of the Total Environment*, 791, undefined-undefined,
823 <https://doi.org/10.1016/j.scitotenv.2021.148277>, 2021.

824 Fialho, P., Hansen, A. D. A., and Honrath, R. E.: Absorption coefficients by aerosols in remote areas: a new approach to
825 decouple dust and black carbon absorption coefficients using seven-wavelength Aethalometer data, *Journal of Aerosol*
826 *Science*, 36, 267–282, <https://doi.org/10.1016/j.jaerosci.2004.09.004>, 2005.

827 Formenti, P., Rajot, J. L., Desboeufs, K., Saïd, F., Grand, N., Chevaillier, S., and Schmechtig, C.: Airborne observations
828 of mineral dust over western Africa in the summer Monsoon season: spatial and vertical variability of physico-chemical
829 and optical properties, *Atmospheric Chemistry and Physics*, 11, 6387–6410, <https://doi.org/10.5194/acp-11-6387-2011>,
830 2011.

831 Freedman, D. and Diaconis, P.: On the histogram as a density estimator:L 2 theory, *Z. Wahrscheinlichkeitstheorie verw*
832 *Gebiete*, 57, 453–476, <https://doi.org/10.1007/BF01025868>, 1981.

833 Hansen, A. D. A., Rosen, H., and Novakov, T.: The aethalometer - An instrument for the real-time measurement of optical
834 absorption by aerosol particles, *Science of the Total Environment*, The, 36, 191–196, 1984.

835 [Heuser, J., Di Biagio, C., Yon, J., Cazaunau, M., Bergé, A., Pangui, E., Zanatta, M., Renzi, L., Marinoni, A., Inomata, S.,](https://doi.org/10.5194/egusphere-2024-2381)
836 [Yu, C., Bernardoni, V., Chevaillier, S., Ferry, D., Laj, P., Maillé, M., Massabò, D., Mazzei, F., Noyalet, G., Tanimoto,](https://doi.org/10.5194/egusphere-2024-2381)
837 [H., Temime-Roussel, B., Vecchi, R., Vernocchi, V., Formenti, P., Picquet Varrault, B., and Doussin, J. F.: Spectral](https://doi.org/10.5194/egusphere-2024-2381)
838 [optical properties of soot: laboratory investigation of propane flame particles and their link to composition,](https://doi.org/10.5194/egusphere-2024-2381)
839 [https://doi.org/10.5194/egusphere-2024-2381, 9 October 2024.](https://doi.org/10.5194/egusphere-2024-2381)Heuser, J., Di Biagio, C., Yon, J., Cazaunau, M., Bergé,
840 [A., Pangui, E., Zanatta, M., Renzi, L., Marinoni, A., Inomata, S., Yu, C., Bernardoni, V., Chevaillier, S., Ferry, D., Laj,](https://doi.org/10.5194/acp-25-6407-2025)
841 [P., Maillé, M., Massabò, D., Mazzei, F., Noyalet, G., Tanimoto, H., Temime-Roussel, B., Vecchi, R., Vernocchi, V.,](https://doi.org/10.5194/acp-25-6407-2025)
842 [Formenti, P., Picquet-Varrault, B., and Doussin, J.-F.: Spectral optical properties of soot: laboratory investigation of](https://doi.org/10.5194/acp-25-6407-2025)
843 [propane flame particles and their link to composition, *Atmospheric Chemistry and Physics*, 25, 6407–6428,](https://doi.org/10.5194/acp-25-6407-2025)
844 [https://doi.org/10.5194/acp-25-6407-2025, 2025.](https://doi.org/10.5194/acp-25-6407-2025)[u1]

845 Hinds, W. C.: *Aerosol Technology: Properties, Behavior, and Measurement of Airborne Particles*, John Wiley & Sons,
846 504 pp., 1999.

- 847 Huang, S.-H., Chen, C.-W., Kuo, Y.-M., Lai, C.-Y., McKay, R., and Chen, C.-C.: Factors Affecting Filter Penetration
848 and Quality Factor of Particulate Respirators, *Aerosol Air Qual. Res.*, 13, 162–171,
849 <https://doi.org/10.4209/aaqr.2012.07.0179>, 2013.
- 850 Kalbermatter, D. M., Močnik, G., Drinovec, L., Visser, B., Röhrbein, J., Oscity, M., Weingartner, E., Hyvärinen, A.-P.,
851 and Vasilatou, K.: Comparing black-carbon- and aerosol-absorption-measuring instruments – a new system using lab-
852 generated soot coated with controlled amounts of secondary organic matter, *Atmospheric Measurement Techniques*, 15,
853 561–572, <https://doi.org/10.5194/amt-15-561-2022>, 2022.
- 854 Kok, J. F., Storelvmo, T., Karydis, V. A., Adebisi, A. A., Mahowald, N. M., Evan, A. T., He, C., and Leung, D. M.:
855 Mineral dust aerosol impacts on global climate and climate change, *Nat Rev Earth Environ*, 4, 71–86,
856 <https://doi.org/10.1038/s43017-022-00379-5>, 2023.
- 857 Lack, D. A., Cappa, C. D., Cross, E. S., Massoli, P., Ahern, A. T., Davidovits, P., and Onasch, T. B.: Absorption
858 Enhancement of Coated Absorbing Aerosols: Validation of the Photo-Acoustic Technique for Measuring the
859 Enhancement, *Aerosol Science and Technology*, 43, 1006–1012, <https://doi.org/10.1080/02786820903117932>, 2009.
- 860 Laing, J. R., Jaffe, D. A., and Sedlacek, A. J.: Comparison of filter-based absorption measurements of biomass burning
861 aerosol and background aerosol at the mt. Bachelor observatory, *Aerosol and Air Quality Research*, 20, 663–678,
862 <https://doi.org/10.4209/aaqr.2019.06.0298>, 2020.
- 863 Laj, P., Bigi, A., Rose, C., Andrews, E., Lund Myhre, C., Collaud Coen, M., Lin, Y., Wiedensohler, A., Schulz, M.,
864 Ogren, J. A., Fiebig, M., Glib, J., Mortier, A., Pandolfi, M., Petäjä, T., Kim, S.-W., Aas, W., Putaud, J.-P., Mayol-Bracero,
865 O., Keywood, M., Labrador, L., Aalto, P., Ahlberg, E., Alados Arboledas, L., Alastuey, A., Andrade, M., Artíñano, B.,
866 Ausmeel, S., Arsov, T., Asmi, E., Backman, J., Baltensperger, U., Bastian, S., Bath, O., Beukes, J. P., Brem, B. T.,
867 Bukowiecki, N., Conil, S., Couret, C., Day, D., Dayantolis, W., Degorska, A., Eleftheriadis, K., Fetfatzis, P., Favez, O.,
868 Flentje, H., Gini, M. I., Gregorič, A., Gysel-Beer, M., Hallar, A. G., Hand, J., Hoffer, A., Hueglin, C., Hooda, R. K.,
869 Hyvärinen, A., Kalapov, I., Kalivitis, N., Kasper-Giebl, A., Kim, J. E., Kouvarakis, G., Kranjc, I., Krejci, R., Kulmala,
870 M., Labuschagne, C., Lee, H.-J., Lihavainen, H., Lin, N.-H., Löschau, G., Luoma, K., Marinoni, A., Martins Dos Santos,
871 S., Meinhardt, F., Merkel, M., Metzger, J.-M., Mihalopoulos, N., Nguyen, N. A., Ondracek, J., Pérez, N., Perrone, M. R.,
872 Petit, J.-E., Picard, D., Pichon, J.-M., Pont, V., Prats, N., Prenni, A., Reisen, F., Romano, S., Sellegri, K., Sharma, S.,
873 Schauer, G., Sheridan, P., Sherman, J. P., Schütze, M., Schwerin, A., Sohmer, R., Sorribas, M., Steinbacher, M., Sun, J.,
874 Titos, G., et al.: A global analysis of climate-relevant aerosol properties retrieved from the network of Global Atmosphere
875 Watch (GAW) near-surface observatories, *Atmospheric Measurement Techniques*, 13, 4353–4392,
876 <https://doi.org/10.5194/amt-13-4353-2020>, 2020.
- 877 Li, J., Carlson, B. E., Yung, Y. L., Lv, D., Hansen, J., Penner, J. E., Liao, H., Ramaswamy, V., Kahn, R. A., Zhang, P.,
878 Dubovik, O., Ding, A., Laci, A. A., Zhang, L., and Dong, Y.: Scattering and absorbing aerosols in the climate system,
879 *Nat Rev Earth Environ*, 3, 363–379, <https://doi.org/10.1038/s43017-022-00296-7>, 2022.
- 880 Liu, D., He, C., Schwarz, J. P., and Wang, X.: Lifecycle of light-absorbing carbonaceous aerosols in the atmosphere, *npj*
881 *Clim Atmos Sci*, 3, 1–18, <https://doi.org/10.1038/s41612-020-00145-8>, 2020a.
- 882 Liu, F., Yon, J., Fuentes, A., Lobo, P., Smallwood, G. J., and Corbin, J. C.: Review of recent literature on the light
883 absorption properties of black carbon: Refractive index, mass absorption cross section, and absorption function, *Aerosol*
884 *Science and Technology*, 54, 33–51, <https://doi.org/10.1080/02786826.2019.1676878>, 2020b.
- 885 Luoma, K., Virkkula, A., Aalto, P., Lehtipalo, K., Petäjä, T., and Kulmala, M.: Effects of different correction algorithms
886 on absorption coefficient – a comparison of three optical absorption photometers at a boreal forest site, *Atmospheric*
887 *Measurement Techniques*, 14, 6419–6441, <https://doi.org/10.5194/amt-14-6419-2021>, 2021.
- 888 Marinoni, A., Cristofanelli, P., Calzolari, F., Roccato, F., Bonafè, U., and Bonasoni, P.: Continuous measurements of
889 aerosol physical parameters at the Mt. Cimone GAW Station (2165 m asl, Italy), *Science of The Total Environment*, 391,
890 241–251, <https://doi.org/10.1016/j.scitotenv.2007.10.004>, 2008.
- 891 Massabò, D., Bernardoni, V., Bove, M. C., Brunengo, A., Cuccia, E., Piazzalunga, A., Prati, P., Valli, G., and Vecchi, R.:
892 A multi-wavelength optical set-up for the characterization of carbonaceous particulate matter, *Journal of Aerosol Science*,
893 60, 34–46, <https://doi.org/10.1016/j.jaerosci.2013.02.006>, 2013.
- 894 Massabò, D., Caponi, L., Bernardoni, V., Bove, M. C., Brotto, P., Calzolari, G., Cassola, F., Chiari, M., Fedi, M. E.,
895 Fermo, P., Giannoni, M., Lucarelli, F., Nava, S., Piazzalunga, A., Valli, G., Vecchi, R., and Prati, P.: Multi-wavelength

- 896 optical determination of black and brown carbon in atmospheric aerosols, *Atmospheric Environment*, 108, 1–12,
897 <https://doi.org/10.1016/j.atmosenv.2015.02.058>, 2015.
- 898 Massoli, P., Murphy, D. M., Lack, D. A., Baynard, T., Brock, C. A., and Lovejoy, E. R.: Uncertainty in Light Scattering
899 Measurements by TSI Nephelometer: Results from Laboratory Studies and Implications for Ambient Measurements,
900 *Aerosol Science and Technology*, 43, 1064–1074, <https://doi.org/10.1080/02786820903156542>, 2009.
- 901 Massoli, P., Keabian, P. L., Onasch, T. B., Hills, F. B., and Freedman, A.: Aerosol Light Extinction Measurements by
902 Cavity Attenuated Phase Shift (CAPS) Spectroscopy: Laboratory Validation and Field Deployment of a Compact Aerosol
903 Particle Extinction Monitor, *Aerosol Science and Technology*, 44, 428–435,
904 <https://doi.org/10.1080/02786821003716599>, 2010.
- 905 Modini, R. L., Corbin, J. C., Brem, B. T., Irwin, M., Bertò, M., Pileci, R. E., Fetfatzis, P., Eleftheriadis, K., Henzing, B.,
906 Moerman, M. M., Liu, F., Müller, T., and Gysel-Beer, M.: Detailed characterization of the CAPS single-scattering albedo
907 monitor (CAPS PMssa) as a field-deployable instrument for measuring aerosol light absorption with the extinction-minus-
908 scattering method, *Atmospheric Measurement Techniques*, 14, 819–851, <https://doi.org/10.5194/amt-14-819-2021>, 2021.
- 909 Moore, R. H., Ziemba, L. D., Dutcher, D., Beyersdorf, A. J., Chan, K., Crumeyrolle, S., Raymond, T. M., Thornhill, K.
910 L., Winstead, E. L., and Anderson, B. E.: Mapping the Operation of the Miniature Combustion Aerosol Standard (Mini-
911 CAST) Soot Generator, *Aerosol Science and Technology*, 48, 467–479, <https://doi.org/10.1080/02786826.2014.890694>,
912 2014.
- 913 Moschos, V., Gysel-Beer, M., Modini, R. L., Corbin, J. C., Massabò, D., Costa, C., Danelli, S. G., Vlachou, A.,
914 Daellenbach, K. R., Szidat, S., Prati, P., Prévôt, A. S. H., Baltensperger, U., and El Haddad, I.: Source-specific light
915 absorption by carbonaceous components in the complex aerosol matrix from yearly filter-based measurements, *Atmos.*
916 *Chem. Phys.*, 21, 12809–12833, <https://doi.org/10.5194/acp-21-12809-2021>, 2021.
- 917 Moteki, N.: Climate-relevant properties of black carbon aerosols revealed by in situ measurements: a review, *Prog Earth*
918 *Planet Sci*, 10, 12, <https://doi.org/10.1186/s40645-023-00544-4>, 2023.
- 919 Moteki, N., Kondo, Y., Nakayama, T., Kita, K., Sahu, L. K., Ishigai, T., Kinase, T., and Matsumi, Y.: Radiative transfer
920 modeling of filter-based measurements of light absorption by particles: Importance of particle size dependent penetration
921 depth, *Journal of Aerosol Science*, 41, 401–412, <https://doi.org/10.1016/j.jaerosci.2010.02.002>, 2010.
- 922 Nakayama, T., Kondo, Y., Moteki, N., Sahu, L. K., Kinase, T., Kita, K., and Matsumi, Y.: Size-dependent correction
923 factors for absorption measurements using filter-based photometers: PSAP and COSMOS, *Journal of Aerosol Science*,
924 41, 333–343, <https://doi.org/10.1016/j.jaerosci.2010.01.004>, 2010.
- 925 Ohata, S., Mori, T., Kondo, Y., Sharma, S., Hyvärinen, A., Andrews, E., Tunved, P., Asmi, E., Backman, J., Servomaa,
926 H., Veber, D., Eleftheriadis, K., Vratolis, S., Krejci, R., Zieger, P., Koike, M., Kanaya, Y., Yoshida, A., Moteki, N., Zhao,
927 Y., Tobo, Y., Matsushita, J., and Oshima, N.: Estimates of mass absorption cross sections of black carbon for filter-based
928 absorption photometers in the Arctic, *Atmospheric Measurement Techniques*, 14, 6723–6748,
929 <https://doi.org/10.5194/amt-14-6723-2021>, 2021.
- 930 Onasch, T. B., Massoli, P., Keabian, P. L., Hills, F. B., Bacon, F. W., and Freedman, A.: Single Scattering Albedo
931 Monitor for Airborne Particulates, *Aerosol Science and Technology*, 49, 267–279,
932 <https://doi.org/10.1080/02786826.2015.1022248>, 2015.
- 933 Petzold, A. and Schönlinner, M.: Multi-angle absorption photometry - A new method for the measurement of aerosol
934 light absorption and atmospheric black carbon, *Journal of Aerosol Science*, 35, 421–441,
935 <https://doi.org/10.1016/j.jaerosci.2003.09.005>, 2004.
- 936 Petzold, A., Ogren, J. A., Fiebig, M., Laj, P., Li, S.-M., Baltensperger, U., Holzer-Popp, T., Kinne, S., Pappalardo, G.,
937 Sugimoto, N., Wehrli, C., Wiedensohler, A., and Zhang, X.-Y.: Recommendations for reporting “black carbon”
938 measurements, *Atmospheric Chemistry and Physics*, 13, 8365–8379, <https://doi.org/10.5194/acp-13-8365-2013>, 2013.
- 939 Ramanathan, V. and Carmichael, G.: Global and regional climate changes due to black carbon, *Nature Geosci*, 1, 221–
940 227, <https://doi.org/10.1038/ngeo156>, 2008.
- 941 Rodriguez, A. A., Rafla, M. A., Welsh, H. G., Pennington, E. A., Casar, J. R., Hawkins, L. N., Jimenez, N. G., de Loera,
942 A., Stewart, D. R., Rojas, A., Tran, M.-K., Lin, P., Laskin, A., Formenti, P., Cazaunau, M., Pangui, E., Doussin, J.-F.,

- 943 and De Haan, D. O.: Kinetics, Products, and Brown Carbon Formation by Aqueous-Phase Reactions of Glycolaldehyde
 944 with Atmospheric Amines and Ammonium Sulfate, *J Phys Chem A*, 126, 5375–5385,
 945 <https://doi.org/10.1021/acs.jpca.2c02606>, 2022.
- 946 [Romshoo, B., Pöhlker, M., Wiedensohler, A., Pfeifer, S., Saturno, J., Nowak, A., Ciupek, K., Quincey, P., Vasilatou, K.,](#)
 947 [Ess, M. N., Gini, M., Eleftheriadis, K., Robins, C., Gaie-Levrel, F., and Müller, T.: Importance of size representation and](#)
 948 [morphology in modelling optical properties of black carbon: comparison between laboratory measurements and model](#)
 949 [simulations, *Atmospheric Measurement Techniques*, 15, 6965–6989, <https://doi.org/10.5194/amt-15-6965-2022>, 2022.](#)
- 950
- 951 Rovira, J., Savadkoohi, M., Chen, G. I., Močnik, G., Aas, W., Alados-Arboledas, L., Artiñano, B., Aurela, M., Backman,
 952 J., Banerji, S., Beddows, D., Brem, B., Chazeau, B., Coen, M. C., Colombi, C., Conil, S., Costabile, F., Coz, E., de Brito,
 953 J. F., Eleftheriadis, K., Favez, O., Flentje, H., Freney, E., Gregorič, A., Gysel-Beer, M., Harrison, R., Hueglin, C.,
 954 Hyvärinen, A., Ivančić, M., Kalogridis, A.-C., Keernik, H., Konstantinos, G., Laj, P., Liakakou, E., Lin, C., Listrani, S.,
 955 Luoma, K., Maasikmets, M., Manninen, H. E., Marchand, N., dos Santos, S. M., Mbengue, S., Mihalopoulos, N., Nicolae,
 956 D., Niemi, J. V., Norman, M., Ovadnevaite, J., Petit, J.-E., Platt, S., Prévôt, A. S. H., Pujadas, M., Putaud, J.-P., Riffault,
 957 V., Rigler, M., Rinaldi, M., Schwarz, J., Silvergren, S., Teinemaa, E., Teinilä, K., Timonen, H., Titos, G., Tobler, A.,
 958 Vasilescu, J., Vratolis, S., Yttri, K. E., Yubero, E., Zíková, N., Alastuey, A., Petäjä, T., Querol, X., Yus-Díez, J., and
 959 Pandolfi, M.: A European aerosol phenomenology – 9: Light absorption properties of carbonaceous aerosol particles
 960 across surface Europe, *Environment International*, 195, 109185, <https://doi.org/10.1016/j.envint.2024.109185>, 2025.
- 961 Samsat, B. H., Stjern, C. W., Andrews, E., Kahn, R. A., Myhre, G., Schulz, M., and Schuster, G. L.: Aerosol Absorption:
 962 Progress Towards Global and Regional Constraints, *Curr Clim Change Rep*, 4, 65–83, [https://doi.org/10.1007/s40641-](https://doi.org/10.1007/s40641-018-0091-4)
 963 [018-0091-4](https://doi.org/10.1007/s40641-018-0091-4), 2018.
- 964 Sand, M., Samsat, B. H., Myhre, G., Gliß, J., Bauer, S. E., Bian, H., Chin, M., Checa-Garcia, R., Ginoux, P., Kipling, Z.,
 965 Kirkevåg, A., Kokkola, H., Le Sager, P., Lund, M. T., Matsui, H., van Noije, T., Olivie, D. J. L., Remy, S., Schulz, M.,
 966 Stier, P., Stjern, C. W., Takemura, T., Tsigaridis, K., Tsyro, S. G., and Watson-Parris, D.: Aerosol absorption in global
 967 models from AeroCom phase III, *Atmospheric Chemistry and Physics*, 21, 15929–15947, [https://doi.org/10.5194/acp-21-](https://doi.org/10.5194/acp-21-15929-2021)
 968 [15929-2021](https://doi.org/10.5194/acp-21-15929-2021), 2021.
- 969 Sandradewi, J., Prévôt, A. S. H., Szidat, S., Perron, N., Alfarra, M. R., Lanz, V. A., Weingartner, E., and Baltensperger,
 970 U.: Using Aerosol Light Absorption Measurements for the Quantitative Determination of Wood Burning and Traffic
 971 Emission Contributions to Particulate Matter, *Environ. Sci. Technol.*, 42, 3316–3323, <https://doi.org/10.1021/es702253m>,
 972 2008.
- 973 Saturno, J., Pöhlker, C., Massabò, D., Brito, J., Carbone, S., Cheng, Y., Chi, X., Ditas, F., Hrabě de Angelis, I., Morán-
 974 Zuloaga, D., Pöhlker, M. L., Rizzo, L. V., Walter, D., Wang, Q., Artaxo, P., Prati, P., and Andreae, M. O.: Comparison
 975 of different Aethalometer correction schemes and a reference multi-wavelength absorption technique for ambient aerosol
 976 data, *Atmospheric Measurement Techniques*, 10, 2837–2850, <https://doi.org/10.5194/amt-10-2837-2017>, 2017.
- 977 Savadkoohi, M., Pandolfi, M., Reche, C., Niemi, J. V., Mooibroek, D., Titos, G., Green, D. C., Tremper, A. H., Hueglin,
 978 C., Liakakou, E., Mihalopoulos, N., Stavroulas, I., Artiñano, B., Coz, E., Alados-Arboledas, L., Beddows, D., Riffault,
 979 V., De Brito, J. F., Bastian, S., Baudic, A., Colombi, C., Costabile, F., Chazeau, B., Marchand, N., Gómez-Amo, J. L.,
 980 Estellés, V., Matos, V., van der Gaag, E., Gille, G., Luoma, K., Manninen, H. E., Norman, M., Silvergren, S., Petit, J.-E.,
 981 Putaud, J.-P., Rattigan, O. V., Timonen, H., Tuch, T., Merkel, M., Weinhold, K., Vratolis, S., Vasilescu, J., Favez, O.,
 982 Harrison, R. M., Laj, P., Wiedensohler, A., Hopke, P. K., Petäjä, T., Alastuey, A., and Querol, X.: The variability of mass
 983 concentrations and source apportionment analysis of equivalent black carbon across urban Europe, *Environment*
 984 *International*, 178, 108081, <https://doi.org/10.1016/j.envint.2023.108081>, 2023.
- 985 Schmid, O., Artaxo, P., Arnott, W. P., Chand, D., Gatti, L. V., Frank, G. P., Hoffer, A., Schnaiter, M., and Andreae, M.
 986 O.: Spectral light absorption by ambient aerosols influenced by biomass burning in the Amazon Basin. I: Comparison
 987 and field calibration of absorption measurement techniques, *Atmospheric Chemistry and Physics*, 6, 3443–3462,
 988 <https://doi.org/10.5194/acp-6-3443-2006>, 2006.
- 989 Sturges, H. A.: The Choice of a Class Interval, *Journal of the American Statistical Association*, 21, 65–66,
 990 <https://doi.org/10.1080/01621459.1926.10502161>, 1926.
- 991 Valentini, S., Barnaba, F., Bernardoni, V., Calzolari, G., Costabile, F., Di Liberto, L., Forello, A. C., Gobbi, G. P.,
 992 Gualtieri, M., Lucarelli, F., Nava, S., Petralia, E., Valli, G., Wiedensohler, A., and Vecchi, R.: Classifying aerosol particles

- 993 through the combination of optical and physical-chemical properties: Results from a wintertime campaign in Rome (Italy),
994 *Atmospheric Research*, 235, 104799, <https://doi.org/10.1016/j.atmosres.2019.104799>, 2020.
- 995 Virkkula, A., Chi, X., Ding, A., Shen, Y., Nie, W., Qi, X., Zheng, L., Huang, X., Xie, Y., Wang, J., Petäjä, T., and
996 Kulmala, M.: On the interpretation of the loading correction of the aethalometer, *Atmospheric Measurement Techniques*,
997 8, 4415–4427, <https://doi.org/10.5194/amt-8-4415-2015>, 2015.
- 998 Vogel, F., Putero, D., Bonasoni, P., Cristofanelli, P., Zanatta, M., and Marinoni, A.: Saharan dust transport event
999 characterization in the Mediterranean atmosphere using 21 years of in-situ observations,
1000 <https://doi.org/10.5194/egusphere-2025-1278>, 27 March 2025.
1001
- 1002 Wang, J., Doussin, J. F., Perrier, S., Perraudin, E., Katrib, Y., Pangui, E., and Picquet-Varrault, B.: Design of a new multi-
1003 phase experimental simulation chamber for atmospheric photochem, aerosol and cloud chemistry research, *Atmospheric*
1004 *Measurement Techniques*, 4, 2465–2494, <https://doi.org/10.5194/amt-4-2465-2011>, 2011.
- 1005 Weingartner, E., Saathoff, H., Schnaiter, M., Streit, N., Bitnar, B., and Baltensperger, U.: Absorption of light by soot
1006 particles: determination of the absorption coefficient by means of aethalometers, *Journal of Aerosol Science*, 34, 1445–
1007 1463, [https://doi.org/10.1016/S0021-8502\(03\)00359-8](https://doi.org/10.1016/S0021-8502(03)00359-8), 2003.
- 1008 Wiedensohler, A., Birmili, W., Nowak, A., Sonntag, A., Weinhold, K., Merkel, M., Wehner, B., Tuch, T., Pfeifer, S.,
1009 Fiebig, M., Fjåraa, A. M., Asmi, E., Sellegri, K., Depuy, R., Venzac, H., Villani, P., Laj, P., Aalto, P., Ogren, J. A.,
1010 Swietlicki, E., Williams, P., Roldin, P., Quincey, P., Hüglin, C., Fierz-Schmidhauser, R., Gysel, M., Weingartner, E.,
1011 Riccobono, F., Santos, S., Gröning, C., Faloon, K., Beddows, D., Harrison, R., Monahan, C., Jennings, S. G., O’Dowd,
1012 C. D., Marinoni, A., Horn, H.-G., Keck, L., Jiang, J., Scheckman, J., McMurry, P. H., Deng, Z., Zhao, C. S., Moerman,
1013 M., Henzing, B., de Leeuw, G., Löschau, G., and Bastian, S.: Mobility particle size spectrometers: harmonization of
1014 technical standards and data structure to facilitate high quality long-term observations of atmospheric particle number
1015 size distributions, *Atmospheric Measurement Techniques*, 5, 657–685, <https://doi.org/10.5194/amt-5-657-2012>, 2012.
- 1016 [Wittmaack, K.: Advanced evaluation of size-differential distributions of aerosol particles, *Journal of Aerosol Science*, 33,](#)
1017 [1009–1025, 2002.](#)
- 1018 Yus-Díez, J., Bernardoni, V., Močnik, G., Alastuey, A., Ciniglia, D., Ivančič, M., Querol, X., Perez, N., Reche, C., Rigler,
1019 M., Vecchi, R., Valentini, S., and Pandolfi, M.: Determination of the multiple-scattering correction factor and its cross-
1020 sensitivity to scattering and wavelength dependence for different AE33 Aethalometer filter tapes: a multi-instrumental
1021 approach, *Atmospheric Measurement Techniques*, 14, 6335–6355, <https://doi.org/10.5194/amt-14-6335-2021>, 2021.
- 1022 Yus-Díez, J., Drinovec, L., Alados-Arboledas, L., Titos, G., Bazo, E., Casans, A., Patrón, D., Querol, X., Gonzalez-
1023 Romero, A., Perez García-Pando, C., and Močnik, G.: Characterization of filter photometer artefacts in soot and dust
1024 measurements – laboratory and ambient experiments using a traceably-calibrated aerosol absorption reference,
1025 *EGUsphere*, 1–26, <https://doi.org/10.5194/egusphere-2024-3995>, 2025.
- 1026 Zhu, C.-S., Qu, Y., Huang, H., Chen, J., Dai, W.-T., Huang, R.-J., and Cao, J.-J.: Black Carbon and Secondary Brown
1027 Carbon, the Dominant Light Absorption and Direct Radiative Forcing Contributors of the Atmospheric Aerosols Over
1028 the Tibetan Plateau, *Geophysical Research Letters*, 48, e2021GL092524, <https://doi.org/10.1029/2021GL092524>, 2021.
- 1029